

Survival Analysis of Intermediate-Mass Black Holes in Dense Star Clusters

MIGUEL A. S. MARTINEZ,^{1,2} ELENA GONZÁLEZ PRIETO,^{1,2} AND FREDERIC A. RASIO^{1,2}

¹ *Department of Physics & Astronomy, Northwestern University, Evanston, IL 60208, USA*

² *Center for Interdisciplinary Exploration & Research in Astrophysics (CIERA), Northwestern University, Evanston, IL 60208, USA*

ABSTRACT

Recently, an intermediate-mass black hole (IMBH) candidate was announced in the Galactic globular cluster Omega Centauri. IMBHs at the lower end of the traditional mass range have also been detected through gravitational-wave transients, though their formation and subsequent growth linking the two mass scales remains a mystery. One way IMBHs may be produced is through the collapse of very massive stars produced by stellar collisions in dense stellar environments. However, IMBHs may be ejected from such environments by either dynamical recoil from binary–single scattering or gravitational-wave recoil following the merger of two black holes. We conduct Newtonian and post-Newtonian binary–single scattering experiments to study dynamical ejection in greater detail. We obtain fits to the probabilities for dynamical ejection, gravitational wave capture, and per-encounter hardening as a function of the binary mass ratio and hardness with respect to its environment. We borrow techniques from survival analysis (commonly used in studies of medicine, epidemiology, engineering, etc.) to develop a model to calculate the probability of IMBH binary ejection vs in-cluster merger. We confirm that the dynamical ejection probability strongly depends on both the mass ratio of the IMBH compared to other BHs in its environment and on the environment’s velocity dispersion. We estimate that for a typical Milky Way globular cluster, IMBHs with mass $\lesssim 10^3 M_\odot$ are unlikely to be retained until the present. Our results also suggest that IMBH mergers with $q \lesssim 0.2$ may be detectable at higher redshifts with future gravitational wave instruments such as the Einstein Telescope and Cosmic Explorer.

1. INTRODUCTION

Intermediate-mass black holes (IMBHs) have masses between 10^2 and $10^5 M_\odot$ and remain elusive (see [Greene et al. 2020](#), for a review). Recently, there has been evidence for the presence of a black hole (BH) with mass $8,200 - 50,000 M_\odot$ at the center of the Milky Way globular cluster (GC) Omega Centauri ([Häberle et al. 2024](#); [Chen et al. 2025](#)). On the other hand, IMBHs have been unambiguously detected through gravitational-wave (GW) transients, such as the recent event GW231123 with component masses of $137 M_\odot$ and $103 M_\odot$ ([Abac et al. 2025](#)). At least one of these BHs falls within the “upper-mass gap,” the predicted range of roughly $40 - 120 M_\odot$ where BHs should not form from isolated single-star evolution because pair-instability processes destroy the progenitor. However, several studies suggest that this region can be pop-

ulated through consecutive stellar collisions (e.g., [Di Carlo et al. 2019](#); [Rizzuto et al. 2021](#); [Kremer et al. 2020a](#); [Banerjee 2020](#); [González Prieto et al. 2024](#)) or hierarchical BH mergers (e.g., [Miller & Hamilton 2002](#); [McKernan et al. 2012](#); [Rodríguez et al. 2018](#); [Antonini et al. 2019](#); [Gerosa & Berti 2019](#); [Fragione et al. 2020](#); [Fragione & Silk 2020](#)), among other mechanisms.

Studies employing both direct N -body or Monte Carlo simulations of GCs show that, depending on the assumed initial conditions, IMBHs can be formed from the direct collapse of very massive stars (VMSs) produced from chains of stellar mergers in clusters, with the final mass of the of the VMSs very sensitive to initial density of the cluster, binary fraction of massive stars, and metallicity (e.g., [Di Carlo et al. 2019](#); [Rizzuto et al. 2021](#); [Kremer et al. 2020a](#); [Banerjee 2020](#); [Weatherford et al. 2021](#); [González et al. 2021](#); [González Prieto et al. 2024](#); [Fujii et al. 2024](#); [Khurana & Chatterjee 2025](#); [Sharma & Rodríguez 2025](#); [Rantala et al. 2025, 2026](#)). This channel has been theorized to produce stars with core masses below the pair-instability regime and oversized hydrogen envelopes, thus avoiding pair instability and instead col-

lapsing into a BH (Spera et al. 2019). The mass of a BH born from the collapse of a VMS progenitor can then be much larger than is typically possible in isolated evolution channels, depending on the assumed fraction of the H envelope that falls back onto the BH (Costa et al. 2022; Ballone et al. 2023).

A key question is whether lower-mass IMBHs ($10^2 - 10^3 M_\odot$) can be retained in their host environment from their formation at early times and continue to grow until the present day. For example, in the case of IMBHs forming from consecutive collisions in GCs, it has been shown that these objects are easily ejected from the clusters due to recoil kicks from both BH mergers and dynamical interactions (González Prieto et al. 2022). However, if lower-mass IMBHs can be retained, it has been shown that they can grow to much larger masses through mergers with stellar-mass BHs and tidal disruption events (Rizzuto et al. 2023; González Prieto et al. 2025). If these objects can be retained in their host environments, they are an interesting source for a number of electromagnetic transient phenomena, including hypervelocity stars (e.g., Brown et al. 2005; Boubert et al. 2018; Koposov et al. 2020), tidal disruption events of stars (Ramirez-Ruiz & Rosswog 2009; Chen & Shen 2018; Kiroğlu et al. 2023), and tidal disruptions of white dwarfs (Haas et al. 2012; MacLeod et al. 2016).

Studies of initial conditions generally find that without an initially large number and density of massive stars, the formation of VMSs through stellar mergers is rare and IMBHs are formed almost entirely through hierarchical mergers. This is problematic because IMBHs which are formed hierarchically from the mergers of other BHs can have very large spin magnitudes, which greatly increases the magnitude of gravitational-wave recoil kicks (e.g., Rodríguez et al. 2019). However, those formed from direct collapse IMBHs may be born with a small or negligible spin magnitude (Fuller & Ma 2019). A recent simulation with initial $N = 10^7$, the largest to date, found that multiple-generation BHs can be formed efficiently in these clusters through hierarchical mergers, but this study, too, finds that the IMBHs produced are eventually ejected (Mai et al. 2025). The simulation conducted for this study had a wall-clock time in excess of 18 months, making more detailed studies of the full parameter space in this range of N and above impractical, even with Monte Carlo methods.

To circumvent these computational difficulties, a large number of studies develop and use semi-analytic methods for the population synthesis of dense stellar clusters to study the properties of BH subsystems (e.g., Antonini & Rasio 2016; Antonini et al. 2019; Fragione & Silk 2020; Fragione et al. 2022; Atallah et al. 2023; Chat-

topadhyay et al. 2023; Kritos et al. 2024). Studies using such methods typically consider one or a population of BH binaries evolving along with a cluster background under Hénon’s Principle of balanced evolution (Breen & Heggie 2013). Most studies find that only clusters with total mass $10^7 M_\odot$ and above, e.g. the most massive GCs or nuclear star clusters, are efficient at retaining IMBHs and facilitating further growth due to their high escape speeds.

A common practice in studies employing semi-analytical methods is to evaluate the probability of ejection by assuming a fixed hardening rate per dynamical encounter and computing a critical semimajor axis a_{ej} below which a typical few-body interaction will eject the target binary. However, we argue that, as binary ejection arises from the tail of the energy-change distribution, this assumption is worth revisiting explicitly using scattering experiments. Furthermore, the scattering experiments conducted in the past—used to calibrate the hardening rates—tended to focus on either the limit where $m_1 = m_2 = m_3$ (e.g., Hut & Bahcall 1983, valid for typical LVK-type BBHs) or $m_1 \approx m_2 \gg m_3$ to study binary SMBH hardening in galactic centers (e.g., Quinlan 1996; Sesana et al. 2006; Rasskazov et al. 2019). Some studies have been conducted looking at an intermediate range of mass ratios (e.g., Sigurdsson & Phinney 1993; Heggie et al. 1996), though they predate the current interest in BH interactions and do not consider the effect of gravitational radiation. More recently, Rando Forastier et al. (2025) studied binary–single interactions of different mass ratios, but were primarily concerned with the calculation of BH mergers rates in more typical stellar environments, which do not produce IMBHs.

In this study, we investigate the impact of both dynamical recoil kicks from binary–single interactions and gravitational-wave recoil kicks on the retention and ejection of IMBHs in dense star clusters by considering a single IMBH–BH binary in a fixed background of single BHs with the same mass as the secondary. Specifically, we seek to find an IMBH–BH mass ratio that is essentially immune to ejection. For this purpose, we conduct a large suite of binary–single scattering experiments at intermediate mass ratios. In Section 2, we describe our numerical methods. In Section 3, we show and describe our numerical results. In Section 4, we discuss the implications of our results on the detection of IMBH candidates as well as for current and future gravitational wave observations. Finally, in Section 5 we summarize our findings.

2. NUMERICAL SETUP AND METHODS

2.1. Setup for Individual Scattering Experiments

In this study we use scattering code `Fewbody` to numerically evaluate the outcomes for different binary–single interactions (Fregeau et al. 2004). As such, we will follow the notations outlined in Fregeau et al. (2004). In the context of binary–single interactions, the binary is denoted with subscript 0 (e.g., a_0 , e_0) and the single is denoted m_1 . When referring to individual members of the binary, the primary is denoted m_{00} and the secondary m_{01} , such that the total mass of the binary $m_0 = m_{00} + m_{01}$.

When considering the Newtonian, point-particle approximation, the outcome depends only on a few dimensionless parameters. The first is the ratio b/a_0 of the Keplerian hyperbolic impact parameter of the single to the binary semimajor axis. The next two are the mass ratio between the objects within the inner binary $q_{\text{in}} = m_{01}/m_{00}$ and between the single and the primary $q_{\text{out}} = m_1/m_{00}$ (equivalently, one could use the mass ratio between the single and the binary). The energy of the encounter is set by the ratio $v_{\text{inf}}/v_{\text{crit}}$ where v_{inf} is the Keplerian relative velocity at infinity and

$$v_{\text{crit}} = \sqrt{\frac{G}{\mu} \frac{m_{00}m_{01}}{a_0}} \quad (1)$$

is the critical velocity for which the total energy in the encounter is 0; here $\mu = m_0m_1/(m_0+m_1)$ is the reduced mass of the objects in the encounter. However, throughout later sections we will instead refer to the closely related ratio $v_{\text{orb}}/v_{\text{inf}}$ for easier physical interpretability, where $v_{\text{orb}}^2 = \frac{Gm_0}{a_0}$ is the circular orbital speed of the binary. When $m_{00} \gg m_{01} = m_1$, v_{crit} reduces to v_{orb} exactly. The relationship between b and the actual distance of closest approach, r_p , must take gravitational focusing into account:

$$b = r_p \sqrt{1 + \frac{2G(m_0 + m_1)}{r_p v_{\text{inf}}^2}}. \quad (2)$$

For a single combination of the parameters $[q_{\text{in}}, q_{\text{out}}, v_{\text{orb}}/v_{\text{inf}}]$, we marginalize over the orbital orientation and phase, the eccentricity of the binary, and the impact parameter in order to create distributions of outcomes. We sample the orientations and phases such that the encounters are isotropic. The binary eccentricity is sampled from a thermal distribution $p(e_0)de_0 = 2e_0de_0$ (Jeans 1919; Heggie 1975). The impact parameter between the binary and the single is limited to a value b_{max} , which is large enough that all outcomes of interest are captured and, for values $b > b_{\text{max}}$, there are only flybys where the binary is weakly perturbed. Because of the geometry of the problem, larger impact parameters are more common

than smaller ones. We sample the impact parameter $p(b)db = 2\pi bdb$. For the value of b_{max} , we use Eq. (2) with

$$r_{p,\text{max}} = 5 a_0. \quad (3)$$

We have verified that for all q considered here our results would not change had we used larger values of $r_{p,\text{max}}$. In principle, in order to be fully self-consistent, it would be necessary to include an eccentricity dependence in this expression when considering individual scattering experiments. However, we elect to neglect this dependence for several reasons. First, it complicates comparisons with previous studies, which do not include any eccentricity dependence. Second, including this dependence would unnecessarily complicate the calculation of cross sections, since we marginalize over a thermal eccentricity distribution. We do not expect this to affect the final outcomes, as we are primarily concerned with large exchanges of energy between the binary and the single. Neglecting the eccentricity dependence in this way only increases the number of perturbative flybys for the relatively rare (near-)circular binaries.

2.2. Outcomes, Cross Sections, and Timescales

The cross section for an outcome X (e.g., a binary energy change greater or less than some value) can be written as

$$\sigma_X = \pi b_{\text{max}}^2 \frac{N_X}{N}, \quad (4)$$

where N is the total number of experiments and N_X is the number which result in an outcome X. In some cases, it is preferable to work with the branching ratios $P_X = N_X/N$, which can be interpreted as the empirical probability for the X. Since these branching ratios are computed numerically, there is some inherent uncertainty in the calculation. The first, from Poissonian counting statistics, is

$$\Delta\sigma_X = \pi b_{\text{max}}^2 \frac{\sqrt{N_X}}{N}. \quad (5)$$

The uncertainty ΔP_X follows similarly. The second, σ_{inc} , comes from encounters that are classified as incomplete due to reaching a wall-clock time limit of 1 hour. σ_{inc} is calculated with Eq. (4) above, so that the total uncertainty

$$\Delta\sigma_{X,\text{tot}} = \Delta\sigma_X + \sigma_{\text{inc}}, \quad (6)$$

but in practice $P_{\text{inc}} \lesssim 10^{-5}$ so that the Poissonian uncertainty usually dominates.

Given σ_X for different outcomes, the relative rates of these outcomes can be estimated with $\Sigma_X \approx n\sigma_X v_{\text{inf}}$. In the hard-binary limit ($v_{\text{orb}} \gg v_{\text{inf}}$) that we consider,

the second term under the radical in Eq. (2) dominates, and this reduces to

$$\Sigma_X = \frac{2\pi n G(m_0 + m_1)r_{p,\max}}{v_{\text{inf}}} \frac{N_X}{N}. \quad (7)$$

Under the hard-binary approximation, we can write the time between encounters, the inverse of the previous expression, as

$$T_{\text{enc}} = \frac{v_{\text{inf}}^3}{10\pi n G^2 m_{00}^2} \left(\frac{v_{\text{orb}}}{v_{\text{inf}}} \right)^2 \frac{1}{(1+q)(1+2q)}. \quad (8)$$

While the outcomes of binary–single interactions are scale-free in isolation, the rates or timescales of interactions depend on the mass scale m_{00} . One factor of m_{00} comes from enhanced gravitational focusing for larger masses. A second comes from the dependence on the physical size of the binary, which we have eliminated in favor of $v_{\text{orb}}/v_{\text{inf}}$. The timescale for an outcome X and its associated uncertainty are then

$$T_X = \frac{N}{N_X} T_{\text{enc}} \quad (9)$$

$$\Delta T_X = T_X \frac{1}{\sqrt{N_X}}.$$

2.3. Escape from Clusters

The previous discussion only considered binary–single encounters in isolation. However, escape can only be defined in relation to the host cluster. We make the approximation that all interactions happen in the center of the cluster core due to efficient mass segregation of the IMBH binary.

For each encounter, we assume that the interaction velocity v_{inf} is equal to the central velocity dispersion σ_{disp} . In doing so, we set the relation between the energy scale of the cluster and the energy scale of the scattering interaction. The relationship between v_{inf} and the escape velocity v_{esc} is determined by the depth and shape of the potential well.

We use a Plummer profile (Plummer 1911), characterized by a radial scale a , with a potential

$$\Phi(r) = -\frac{GM_{\text{tot}}}{\sqrt{r^2 + a^2}}.$$

From the potential, the density

$$\rho(r) = \frac{3M_{\text{tot}}}{4\pi a^3} \left(1 + \frac{r^2}{a^2} \right)^{-5/2}, \quad (10)$$

velocity dispersion

$$\sigma_{\text{disp}}^2(r) = -\frac{\Phi(r)}{6}, \quad (11)$$

and escape velocity

$$v_{\text{esc}}(r) = \sqrt{-2\Phi(r)} = \sqrt{12}\sigma_{\text{disp}}(r) \quad (12)$$

can be found (e.g., Binney & Tremaine 2008). In general, the velocities v_{inf} , σ_{disp} , and v_{esc} are related by numerical coefficients whose values are determined by the structure of the cluster potential. In Section 3.2, we will explore the impact of different choices for the potential.

To determine P_{ej} , the fraction of objects which are ejected, we compare v_{esc} with v_{kick} , the magnitude of the dynamical recoil from a binary–single interaction. In order to calculate v_{kick} , we first compute the magnitude of the new relative velocity from infinity

$$v_{\text{inf}}'^2 = \frac{m_0 m_1}{m_0' m_1'} v_{\text{inf}}^2 + \frac{2(m_0 + m_1)E_0 \Delta}{m_0' m_1'} \quad (13)$$

where the primed masses denote the masses of the binary and the single following the interaction, as they may be different due to an exchange interaction, E_0 is the initial energy of the binary (e) and

$$\Delta = \frac{E_0 - E_0'}{E_0} \quad (14)$$

is the fractional change in the total energy of the binary following the interaction (we have the notation of Equations 4.1 and 4.3 of Sigurdsson & Phinney 1993). With this definition, $\Delta < 0$ if a binary is hardened and $\Delta > 0$ if it is softened. Finally, v_{kick} for the binary follows from Eq. (13) and momentum conservation:

$$v_{\text{kick}} = \frac{m_1'}{m_0' + m_1'} v_{\text{inf}}'. \quad (15)$$

A similar expression exists for the single.

2.4. Triple Formation and Destruction

In a binary–single encounter without dissipative forces, it is impossible for a stable triple to form as a consequence of time reversal symmetry (Chazy 1929). However, in analogy to the formation of a tidal capture binary, temporarily bound triple systems can be formed during extremely long-lived resonance interactions (Bailyn 1989). For this reason, Fewbody reports a small but non-negligible triple formation cross section for large values of $v_{\text{orb}}/v_{\text{inf}}$. Fewbody determines the stability of a triple using the criterion (Mardling & Aarseth 2001)

$$\frac{a_{\text{out}}}{a_{\text{in}}} > \frac{3.3}{1 - e_{\text{out}}} \left[\frac{2}{3} \left(1 + \frac{m_{\text{out}}}{m_{\text{bin}}} \right) \times \frac{1 + e_{\text{out}}}{(1 - e_{\text{out}})^{1/2}} \right]^{2/5} (1 - 0.3I/\pi), \quad (16)$$

where in this notation a_{in} is the semimajor axis of the inner binary with mass m_{bin} , a_{out} and e_{out} are the semimajor axis and eccentricity of the outer binary between m_{bin} and the tertiary m_{out} , and I is the mutual inclination between the two orbits. The “stable” triples reported by this criterion are, by construction of the scattering experiments, spurious in the sense that they are only metastable. This seeming contradiction is due to the construction of the stability criterion itself. This and later criteria (e.g., [Lalande & Trani 2022](#); [Hayashi et al. 2022, 2023](#)) have been developed empirically through the use of extensive N-body modeling in order to determine the boundary between stability and instability. However, since all 3-body systems are chaotic, it is possible that the dissolution timescale for systems that fit these criteria on paper are much longer than the integration time used in these studies.

In principle, the production of hierarchical triples in our simulations represents a numerical uncertainty inherent to the classification system and should be included in the computational uncertainty budget of Eq. (6). However, in light of the discussion above, we could instead argue for a few different resolutions. On one hand, we can assume that these triples will be quickly ionized by the stellar environment and simply break them up, similar to the phenomenon highlighted by [Ginat & Perets \(2021\)](#). On the other hand, we can assume that eventually these triples will dissolve due to energy exchange. In this case, we can assume that the outer orbit will be ionized by extracting energy from the inner orbit. We check two different cases: first, we assume a negligible energy change $v'_{\text{inf}} = v_{\text{inf}}$. Second, we assume that the encounter terminates with a perfectly parabolic encounter such that $v'_{\text{inf}} = 0$, having softened the binary by the maximum possible amount. Regardless, we would not expect this to radically change σ_{ej} , which depends on the binary having hardened. However, it is possible that this could affect the per-encounter mean hardening rate we compute in Section 3.3.

For constructing our results, we choose the first option, since, when including post-Newtonian dissipation as we do in Section 3.4, there is a small number of cases where significant dissipation occurs resulting in the formation of a truly stable triple system. These cannot be disentangled from the majority of cases where a likely misclassification occurred. We find that choosing between any of the first three cases results in no statistically significant difference in the results that follow.

3. RESULTS

In this section, we present results from numerical scattering experiments. We assume that a binary with

primary mass m_{00} and secondary mass $m_{01} = qm_{00}$ is in a fixed background of single masses $m_1 = m_{01}$. We conduct scattering experiments over a grid with $q = [0.01, 0.02, 0.03, 0.06, 0.1, 0.2, 0.3, 0.6]$ and a range $v_{\text{inf}}/v_{\text{crit}} = 10^{-4} - 10$ with 71 points evenly spaced logarithmically. For each point in $(q, v_{\text{inf}}/v_{\text{crit}})$ space, we conduct $\mathcal{O}(10^4)$ scattering experiments.

Except where otherwise indicated, calculations for dimensionful quantities are done with fiducial values $m_{00} = 100 M_{\odot}$, $n = 10^6 \text{ pc}^{-3}$, and $\sigma_{\text{disp}} \approx v_{\text{inf}} = 20 \text{ km/s}$. This density and dispersion is representative for young massive clusters based on the early-time properties of the models presented in [Kremer et al. \(2020b\)](#); [González Prieto et al. \(2022\)](#). With this σ_{disp} , $v_{\text{esc}} \approx 70 \text{ km/s}$ for a Plummer sphere.

3.1. Key Physical Parameters

Here, we discuss how the distribution of the binary fractional energy change Δ and therefore of v_{kick} is affected by some key physical parameters describing the interaction.

The first key parameter is the binary hardness, which is characterized by the ratio $v_{\text{orb}}/v_{\text{inf}}$. This parameter characterizes the internal energy of the binary with respect to the kinetic energy of the single object. With our imposition $v_{\text{inf}} = \sigma_{\text{disp}}$, the hardness parameter characterizes the energy scale of the binary with respect to the thermal energy of the cluster. In Figure 1, we show the influence of the hardness of the binary on the distributions v_{kick} (left panel, cumulative density functions) and $-\Delta$ (right panel, probability density functions). Both sets of scattering experiments have the same mass ratio $q = 0.6$ but different hardness parameters, with the solid green lines corresponding to the softer binary and the dashed purple lines to the harder binary. The dotted line in the top panel shows the value of the escape boundary for the cluster in the dimensionless units $v_{\text{kick}}/v_{\text{orb}}$ for each value of hardness. Objects to the right of this boundary can be said to escape. For convenience, we also state in the caption the semimajor axis of the binaries in each set of scattering experiments, assuming our fiducial m_{00} and v_{inf} .

For the case of a hard binary, the energy of the incoming single is negligible with respect to the energy of the binary. As a result, the PDFs shown in the bottom panel are roughly the same, with much of the difference occurring in the low-probability tail of the distribution. The v_{kick} CDFs in the top panel are also roughly the same, with the high-velocity tail corresponding to the tail in the Δ distributions. Changing the value of the hardness parameter results in the escape boundary shifting to a higher or lower value. For the softer green distribution,

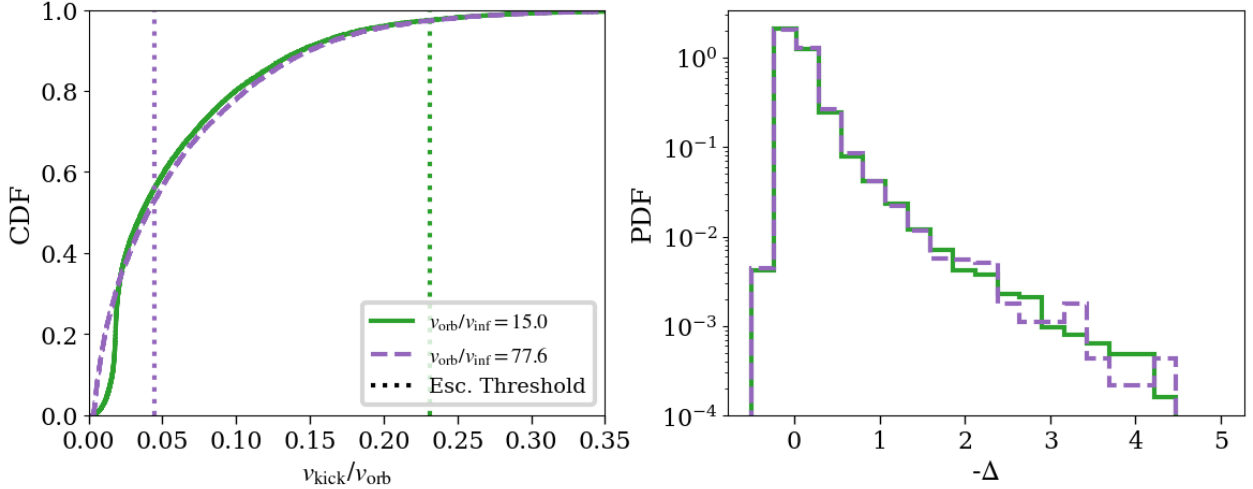


Figure 1. (Left) Cumulative distributions of binary $v_{\text{kick}}/v_{\text{orb}}$ for different values of binary hardness $v_{\text{orb}}/v_{\text{inf}}$. The vertical dashed lines shows the escape speed of the background cluster in the corresponding normalized units for the CDF of the same color. Binaries with kick velocities to the right of this line are ejected. (Right) Normalized distributions of the fractional change of the binary Δ as a result of the interaction for the same selected values of $v_{\text{orb}}/v_{\text{inf}}$. Both sets of distributions show results from $q = 0.6$ scattering experiments. In physical units, these selected values of $v_{\text{orb}}/v_{\text{inf}}$ correspond to $100 M_{\odot}$ – $60 M_{\odot}$ binaries with semimajor axis $a_0 = 1.6$ au (solid green) and $a_0 = 0.06$ au (dashed purple) for $v_{\text{inf}} = 20$ km/s. In the limit $v_{\text{crit}} \gg v_{\text{inf}}$, the distribution of Δ converges to a single distribution. Thus, in the normalized units used here, making the binary harder or softer corresponds to changing the boundary for escape. For relatively soft binaries (green), the possibility of escape lies only in the tail of the recoil kick distribution, whereas for harder binaries (purple), escape may be possible in the bulk of the distribution.

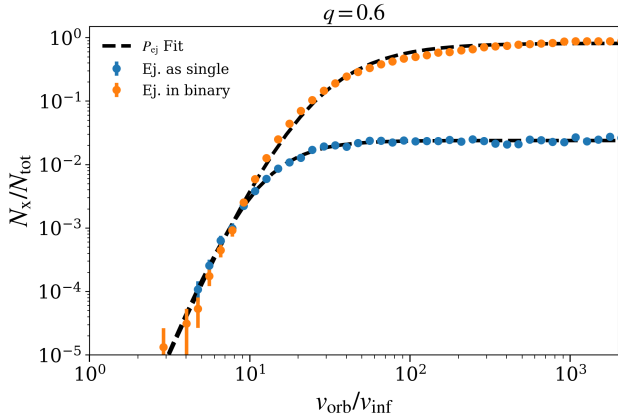


Figure 2. Branching ratios for ejection of the most massive BH in our $q = 0.6$ interactions as a function of $v_{\text{orb}}/v_{\text{inf}}$. In most cases, the BH will be ejected as part of a binary (orange points), though in a minority of cases it may be ejected as a single object (blue points). We show the fit from Eq. (17) in black. The fit parameters for the fit to the binary ejection probability are provided in Tab. 1.

the escape boundary is in the tail of the distribution, so only a few percent of the binaries here have escaped the cluster, whereas for the harder purple distribution, the boundary has moved into the bulk, so the escape fraction is approximately 45%.

In Figure 2, we show the ejection branching ratio for $q = 0.6$ as a function of $v_{\text{orb}}/v_{\text{inf}}$. In most cases, the

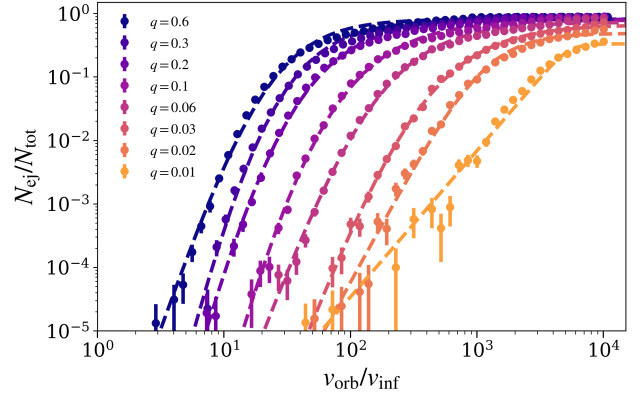


Figure 3. Branching ratios for ejection of the massive object in a binary for all simulated mass ratios (diamonds) with fits (dashed lines). Fit parameters are provided in Tab. 1.

most massive object is ejected as part of a binary (orange points), but in a minority of cases it is possible that it is ejected as a single object (blue points). The different data and fits correspond to the highest (left-most) to the lowest (right-most) mass ratios simulated. In general, the probability for ejection of the most massive object as a single is negligible, so that in following sections, we define P_{ej} and the associated cross sections and timescales to refer only to cases where the most massive object is ejected as part of the final binary. This preference arises from the usual heuristic that there is

q	A	w	n	p
0.6	0.81	21	1.5	5.8
0.3	0.78	20	1.4	8.3
0.2	0.81	26	1.2	7.9
0.1	0.79	44	1.1	8.3
0.06	0.73	1.4×10^2	1.2	5.6
0.03	0.67	3.5×10^2	1.2	5.3
0.02	0.49	1.2×10^3	2.0	3.7
0.01	0.33	5.4×10^3	6.8	2.3

Table 1. Fit parameters for Eq. (17).

an energetic preference that the lightest object involved becomes the single following a strong interaction (e.g., Heggie et al. 1996). Furthermore, for constant Δ , v_{kick} is smaller when the massive object is ejected as a single by inspection of Eq. (13) and Eq. (15) compared to when it is ejected as part of the binary. This difference between the two branching ratios becomes more stark with lower values of q , which is already quite dramatic for the largest q tested.

In Figure 3, we show the branching ratio for ejection in the binary for all mass ratios as a function of $v_{\text{orb}}/v_{\text{inf}}$. In both figures, we also present a fit of the form

$$P_{\text{ej}} = A \left[1 + \left(\frac{w}{\tilde{v}} \right)^n \right]^{-p/n} \quad (17)$$

where $\tilde{v} = v_{\text{orb}}/v_{\text{inf}}$. Fit parameters¹ are given for all mass ratios in Table 1. The different parameters have the following interpretation. At low \tilde{v} , the function behaves as \tilde{v}^{-p} , whereas at high \tilde{v} it saturates to the amplitude A . Then, w is approximately the location where the transition occurs, and n controls the sharpness of the transition. The velocity at which it becomes probable for the binary to be ejected (say, $P_{\text{ej}} \gtrsim 10\%$) moves further to the right with decreasing q , as expected.

One point of interest is the importance of resonant interactions, which are named in analogy to particle physics. Resonant interactions refer to those interactions which are long-lived compared to the typical crossing time of the interaction $T_{\text{int}} = a_0/v_{\text{inf}}$. Such interactions are long-lived as a result of the formation of temporary hierarchical triples punctuated by democratic phases where there is no clear hierarchy. However, there is no clear threshold in time separating the non-resonant and resonant interactions. For this reason, an alternative definition is sometimes used based

on counting the number of local minima of the sum of the squared pairwise distances between the objects in the interaction (McMillan & Hut 1996), but the threshold used in counting the minima with this definition is also somewhat arbitrary. In any case, in the near equal-mass limit, there is an expectation for a clear divergence in the behavior of the interactions which are long-lived and those which are not (Hut & Bahcall 1983; Manwadkar et al. 2020; Trani et al. 2024).

In Figure 4, we show in the left panel the distribution of simulation times normalized by T_{int} , and in the right panel the distribution of normalized v_{kick} for scattering experiments with $q = 0.2$ and $v_{\text{orb}}/v_{\text{inf}} \approx 73$. In either panel, the solid blue histogram corresponds to the distribution containing all interactions, whereas the dashed orange histograms only includes a subset of interactions for which $\Delta \leq -0.1$ (left) or simulation times $T_{\text{final}} \geq 10 T_{\text{min}}$ (right), where T_{min} is defined as the simulation time for a pure two-body hyperbolic encounter, which depends on the tidal perturbation δ parameter set in **Fewbody**. The results are not sensitive to the exact value of the threshold $10 T_{\text{min}} \approx 100 T_{\text{int}}$, which was simply chosen to safely exclude all the shortest-lived interactions. The spike in the left panel for large values of T_{final} corresponds to a typical orbital period for wide triples formed from an initially-softening encounter. The results presented here are only for one set of simulations but the qualitative features are generic to all the simulations we ran.

However, this does not seem to be the case here, as shown by the equality in the two sets of histograms. A detailed investigation for why this is the case is outside the scope of this work, though we offer some speculation. We can understand this result intuitively in the following way: as these resonant interactions involve a weak perturbation resulting in a very wide triple, subsequent outer pericenter passes will likely result in similarly weak perturbations. This eventually diffuses into the a configuration where the outer object is ionized. For a terminal close encounter to result in some large kick, some degree of luck is still involved. Incidentally, the described process is exactly equivalent to the conditions required to generate a Lévy flight, which produces the power-law distribution seen in the right panel of Fig. 4 (Manwadkar et al. 2020).

3.2. Dependence on Background Cluster Potential

As stated previously, the results shown thus far have assumed a Plummer potential for the background cluster. While the Plummer profile is valued for its simplicity, it is unfortunately unrealistic. For instance, the Plummer model does not have a tidal cutoff radius, un-

¹ While the fits provided are adequate for the purpose of this study, we caution against quoting the exact numerical values for theoretical work. Because the low velocity tail is undersampled, the parameters are somewhat degenerate.

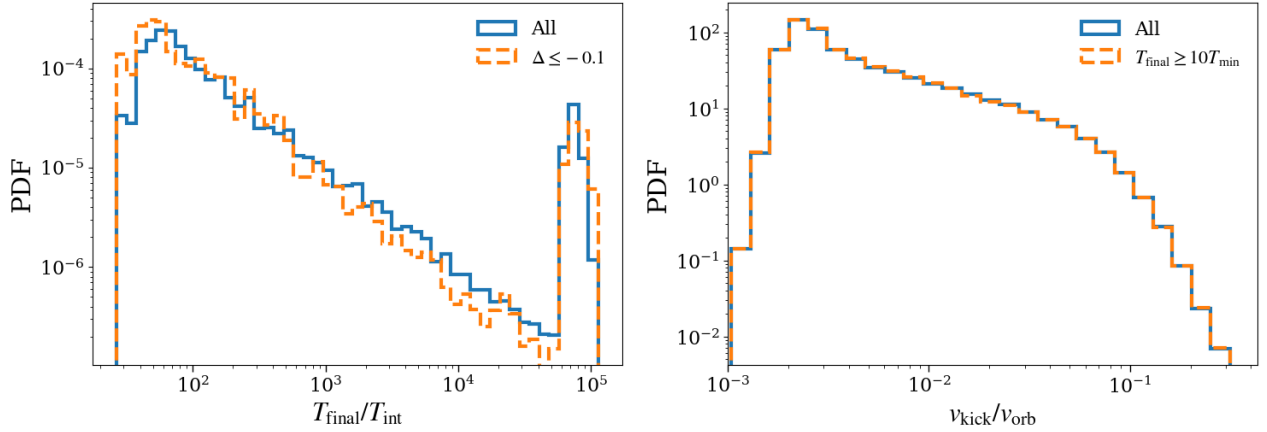


Figure 4. Distributions of $T_{\text{final}}/T_{\text{int}}$ (left) and normalized v_{kick} (right) for all interactions (solid blue) and subsets of the interactions (dashed orange) with $q = 0.2$ and $v_{\text{orb}}/v_{\text{inf}} \approx 73$. In the left panel, the subset includes only interactions for which the change in energy $\Delta \leq -0.1$, whereas in the right panel, it includes only interactions for which $T_{\text{final}} \geq 10T_{\text{min}}$.

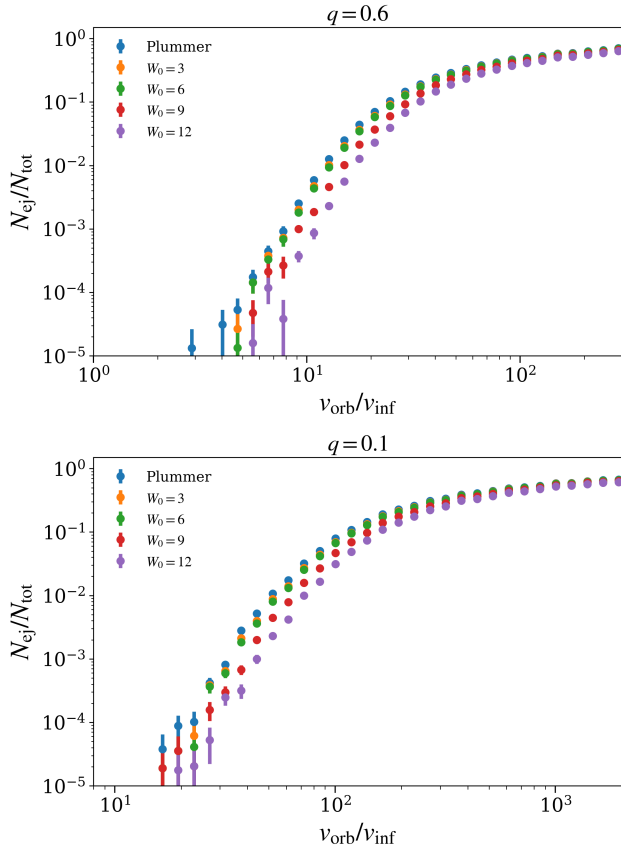


Figure 5. Branching ratios for mass ratios $q = 0.6$ (top) and $q = 0.1$ (bottom) with different assumptions of the background cluster potential as a function of binary hardness. The Plummer model is shown in blue. The King models are shown in green, orange, red and purple with their associated $W_0 = 3, 6, 9, 12$ respectively. The range of W_0 values chosen correspond to a representative range of measured concentration parameters $c = \log(r_t/r_0)$ reported by the Harris catalog of Milky Way GCs (Harris 1996).

like observed clusters. A more realistic model is the family of King profiles (King 1962), which is commonly used to characterize Milky Way GCs (e.g., Harris 1996). In Appendix A, we derive the escape speed and velocity dispersion of a King profile as a function of the parameter W_0 , which characterizes the central depth of the cluster’s potential well. We compare the probability of escape between these different models for the potential.

In Figure 5, we show escape branching ratios as a function of hardness for both $q = 0.6$ and $q = 0.1$. In both panels, it is apparent using a Plummer profile results in the least conservative (i.e. largest) estimate for P_{ej} . The difference between the least conservative estimate and the most conservative estimate (King profile with $W_0 = 12$) is smallest for the hard binaries and less asymmetric mass ratios, as these conditions lead to more interactions which result in recoil kicks with larger magnitude than the escape speed. The difference is more apparent for softer binaries. In the most extreme cases, a branching ratio of 0 is reported for the $W_0 = 12$ criterion whereas other criteria report a non-zero branching ratio. However, as the reported cross section is already minimal in these cases, the difference does not greatly impact the reported results. Additionally, the differences in the cross section between the Plummer, $W_0 = 3$, and $W_0 = 6$ profiles are order unity across all values of $v_{\text{orb}}/v_{\text{inf}}$. However, the shape of the curves, specifically the slope of the power-law, do not seem to change, so that the value for w reported in Tab. 1 is different only by a constant factor.

3.3. Hardening

The ejection timescale implied by Eq. (9) is not quite correct, since it implicitly assumes that the binary stays at a fixed a_0 (or equivalently, a fixed $v_{\text{orb}}/v_{\text{inf}}$). However, the encounters that do not eject the binary will

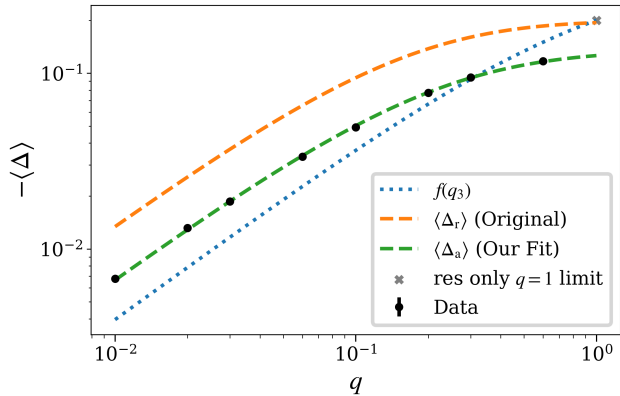


Figure 6. Average per-encounter change in binding energy $-\langle\Delta\rangle$ as a function of q in the hard-binary limit. Fits (black circles) are done from the point where $\langle\Delta\rangle$ approaches a constant value, with error bars smaller than the points. For comparison, we show functions from the literature, namely Eq. (18) from Chattopadhyay et al. (2023) (dotted blue), Eq. (19) from Rando Forastier et al. (2025) (dashed green), and the value from Hut & Bahcall (1983) which was found for resonant interactions in the equal-mass case (grey x). We also refit Eq. (19) using our data for all interactions (dashed orange).

still on average harden the target binary by some small but fixed amount.

We find that in the hard-binary limit, the per-encounter average hardening $\langle\Delta\rangle$ is constant for fixed q , consistent with previous studies. This follows from the fact that the kinetic energy of the single is negligible compared to the internal energy of the binary. For each q , we perform the straight-line fits in the hard-binary regime and present the results as the black circles in Figure 6. The uncertainty in the fit is of the order $\sigma \sim 10^{-4}$, such that the error bars are smaller than the points. We also show the usual assumption for the $q = 1$ case, that in the equal-mass limit $\langle\Delta\rangle = -0.2$ for resonant encounters (gray x) (Hut & Bahcall 1983).

For the sake of comparison, we show two different functions from the literature. First, Chattopadhyay et al. (2023), for use in their semi-analytic code, propose a function of the form

$$f(q_3) = -0.4 \frac{q_3}{1 - q_3} \quad (18)$$

with $q_3 = m_1/(m_0 + m_1) = q/(1 + 2q)$, where the prefactor was chosen to converge to the result found in scattering experiments conducted in the equal mass case (gray x). The function does not reflect the functional form of the data, though it is still correct within a factor of a few.

Second, we compare to the function found in the study by Rando Forastier et al. (2025),

$$\langle\Delta_r\rangle = -\Delta_0 \left[1 - \exp\left(-A \frac{m_1}{m_0}\right) \right] \quad (19)$$

with $\Delta_0 = 0.2$ (to match Hut & Bahcall (1983)) and $A = 7$, where the subscript indicates that this fit was done for *only resonant* interactions. At some level, the comparison is not quite valid, as we perform the average over *all* interactions, whereas theirs is for only the resonant interactions. However, our discussion of Fig. 4 above shows that this should not make a significant difference. The apparent disagreement is also not a concern, since Rando Forastier et al. (2025) fit this function for the condition $m_1 \leq m_0$, whereas our choice of parameters is much more restricted. Looking at their Fig. 1, we see a similar range of disagreement. Nevertheless, the functional form looks similar to our averages over all data, motivating us to fit our own function $\langle\Delta_a\rangle$, where the subscript indicates that this fit is done for *all* interactions. We find

$$\langle\Delta_a\rangle = -0.14 \left[1 - \exp\left(-5 \frac{m_1}{m_0}\right) \right]. \quad (20)$$

3.4. Relativistic Effects

At 2.5 Post-Newtonian (PN) order, the binary systems experience gravitational-wave radiation reaction, causing the binary to slowly shrink until the two objects merge. The inspiral time of a binary is given by the equation (Peters 1964):

$$T_{\text{GW}} = \frac{12}{19} \frac{c_0^4}{\beta} \int_0^{e_0} \frac{e^{29/19} [1 + (121/304)e^2]^{1181/2299}}{(1 - e^2)^{3/2}} de.$$

The constants c_0 and β are

$$c_0 \equiv a_0 e_0^{-12/19} (1 - e_0^2) \left[1 + \frac{121}{304} e_0^2 \right]^{-870/2299}$$

and

$$\beta \equiv \frac{64}{5} \frac{G^3 m_{00} m_{01} m_0}{c^5}.$$

In terms of v_{orb} and q , this may be rewritten as

$$T_{\text{GW}} = \frac{15}{304} G m_{00} c^5 v_{\text{orb}}^{-8} \frac{(1 + q)^3}{q} F(e_0) \quad (21)$$

where $F(e_0)$ is a function of the initial eccentricity e_0 :

$$F(e_0) = \left(e_0^{-12/19} (1 - e_0^2) \left[1 + \frac{121}{304} e_0^2 \right]^{-\frac{870}{2299}} \right)^4 \times \int_0^{e_0} \frac{e^{29/19} [1 + (121/304)e^2]^{1181/2299}}{(1 - e^2)^{3/2}} de$$

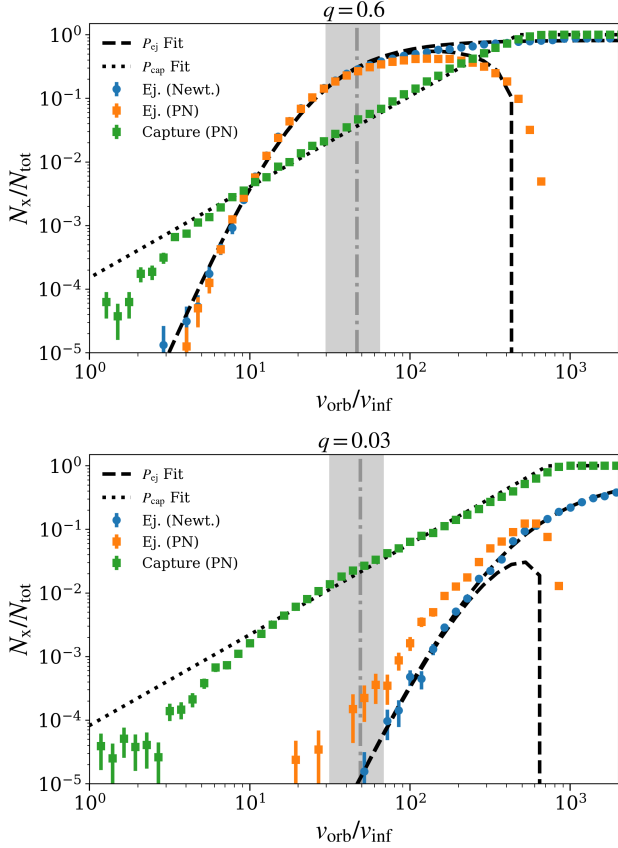


Figure 7. Branching ratios for $q = 0.6$ (top) and $q = 0.03$ (bottom) scattering experiments including PN terms and $v_{\text{inf}} = 20$ km/s. The branching ratios for ejection and merger are shown with orange and green squares, respectively. The Newtonian data from Fig. 3 are replotted (blue circles) for comparison. We also show the fit to P_{cap} with Eq. (22) with $B = 2.61$ (dotted black lines). We attempt to match the PN ejections by combining a simple cutoff with the fit to the Newtonian data (dashed black lines), though this fails for $q \lesssim 0.03$. Finally, the grey shaded areas correspond to the limit $T_{\text{enc}}/T_{\text{GW}} = 1$ (Eq. 23) for $e_0 = 0 - 0.9$, with the dash-dotted line corresponding to $e_0 = 0.7$, roughly the median of the thermal distribution. To compute these timescales we assume $m_{00} = 100 M_{\odot}$ and $n = 10^6 \text{ pc}^{-3}$.

for $0 < e_0 < 1$ and $F(0) = 19/48$.

We conduct additional scattering experiments with 2.5PN terms for all values (q, v) for comparison. We exclude the conservative 1PN and 2PN terms as they are not expected to affect on the cross sections of interest when secular effects are unimportant (Rodriguez et al. 2018). In order to detect mergers between objects, we assign each object an effective radius $10M$ in gravitational units.

There are two effects relevant for this study. First, similar to other finite-size effects, gravitational-wave radiation imposes an effective radius for each of the ob-

jects, such that mergers between objects can occur if they pass close enough for an impulsive, large emission of gravitational radiation. During resonant encounters, repeated interactions between the three objects allow the inner binary to ergodically explore its allowed phase space. Some of the possible configurations result in high eccentricities leading to a prompt GW-induced inspiral, resulting in mergers even when the typical velocities involved are non-relativistic (Samsing et al. 2014). From this, we can write the probability of a merger during a binary–single encounter, typically referred to as a capture, as (Samsing 2018; Rando Forastier et al. 2025)

$$P_{\text{cap}} \simeq B \langle N_{\text{IMS}} \rangle \frac{2r_{\text{GW}}}{a_0} \quad (22)$$

$$\simeq 5.36 B \langle N_{\text{IMS}} \rangle q^{2/7} (1+q)^{-4/7} \left(\frac{v_{\text{orb}}}{c} \right)^{10/7}$$

where $\langle N_{\text{IMS}} \rangle$ is the number of intermediate hierarchical triple states in a resonant encounter and r_{GW} is the pericenter distance at which a single passage radiates energy equal to E_0 (Hansen 1972). We also include a constant B to fit to the data. In principle, $\langle N_{\text{IMS}} \rangle$ is a function of the mass ratios. In the equal-mass case, $\langle N_{\text{IMS}} \rangle \simeq 20$ (Samsing 2018), but in the case $m_{00} > m_{01} = m_1$, $\langle N_{\text{IMS}} \rangle \simeq 15$ for $0.1 \lesssim q \lesssim 0.6$ (Rando Forastier et al. 2025). When $m_{01} \neq m_1$, $\langle N_{\text{IMS}} \rangle$ can be much lower, such that our results are somewhat overpredicting the probability of captures (for additional discussion see Rando Forastier et al. 2025).

Second, we compare T_{GW} to T_{enc} . If the quantity

$$\frac{T_{\text{enc}}}{T_{\text{GW}}} = \frac{304}{150\pi} \frac{v_{\text{inf}}^6}{nG^3 m_{00}^3} \left(\frac{v_{\text{inf}}}{c} \right)^5 \left(\frac{v_{\text{orb}}}{v_{\text{inf}}} \right)^{10} \quad (23)$$

$$\times \frac{q}{(1+q)^4 (1+2q)} \frac{1}{F(e_0)}$$

is larger than 1, then, on average, the binary will merge before experiencing its next encounter.

In Figure 7, we show branching ratios for ejection (orange squares) and merger (green squares) for scattering experiments including 2.5PN terms with $v_{\text{inf}} = 20$ km/s for $q = 0.6$ (top panel) and $q = 0.03$ (bottom panel). The Newtonian ejection branching ratios previously shown in Fig. 3 are shown for comparison (blue circles). We show with dashed black lines fits to both the PN data (described below) and the Newtonian data (from Tab. 1). We also show the fit to Eq. (22). Finally, we show a grey shaded region where $T_{\text{enc}}/T_{\text{GW}} = 1$ for $e_0 = 0 - 0.9$, with the dash-dotted line corresponding to $e_0 = 0.7$. To compute T_{enc} , we assume $m_{00} = 300 M_{\odot}$ and $n = 10^6 \text{ pc}^{-3}$.

We find that the probability for merger during the encounter follows the expected $P \propto v^{10/7}$ scaling for all

mass ratios tested, but only for sufficiently hard velocities ($v_{\text{orb}}/v_{\text{inf}} \gtrsim 3$). However, we find that $B = 2.61$ is required for Eq. (22) to fit the amplitudes. There is still some q dependence that is not captured by this constant factor, but with this value of B , Eq. (22) is correct to within 10% for the range of q simulated. Note that Rando Forastier et al. (2025) found that $\langle N_{\text{IMS}} \rangle$, and therefore P_{merge} , is maximized when $m_{01} = m_1$. As a result, when considering more realistic BH mass functions where the two small masses close but unequal, P_{cap} will be lower by a factor of at most a few, or lower by about an order of magnitude when they are unequal.

Comparing the Newtonian and PN ejection probabilities, we see that in the top panel, the probability stays roughly the same until a divergence at roughly $\tilde{v} \approx 60$, followed by a sudden drop-off when P_{cap} begins to approach unity. We find that the PN P_{ej} is well described by taking the fit to the Newtonian data (upper dashed black lines) as reported in Tab. 1 and including a coefficient $1 - P_{\text{cap}}$ (lower dashed black lines). Indeed, in the top panel, the discrepancy begins to be apparent by eye when $P_{\text{cap}} \approx 0.1$. However, this fix is slightly inadequate for $P_{\text{cap}} \simeq 1$. This is because P_{cap} is appropriate for the high-eccentricity limit, but not when $T_{\text{GW}}(e_0 = 0)$ is comparable to the interaction length. However, for $q \lesssim 0.03$, we find that the ejection probability actually increases for constant $v_{\text{orb}}/v_{\text{inf}}$ when compared to the Newtonian case. This discrepancy arises because, for small q , ejection is only possible when the binary is initially very hard. This also increases the amount of hardening via GW radiation during long resonant encounters, such that the final binary is even harder than the initial state, resulting in a larger v_{kick} . However, the binary will generally merge between successive encounters prior to the point at which PN terms significantly impact the ejection probability. Thus, we can treat the two branching ratios P_{ej} and P_{cap} as independent.

3.5. Survival Analysis for Ejected Binaries

Survival analysis is a set of statistical techniques used to analyze the time until events of interest and is commonly used in fields such as epidemiology, medicine, and engineering. We provide a brief introduction to the subject in Appendix B for readers who are unfamiliar with these techniques.

In order to evaluate the probability of a given outcome occurring, it is not sufficient to compare the timescales or cross sections calculated from the above scattering experiments as there are three separate outcomes that scale differently with $v_{\text{orb}}/v_{\text{inf}}$. Furthermore, the three outcomes are mutually exclusive, which in the language of survival analysis is described as *censoring*; if a binary

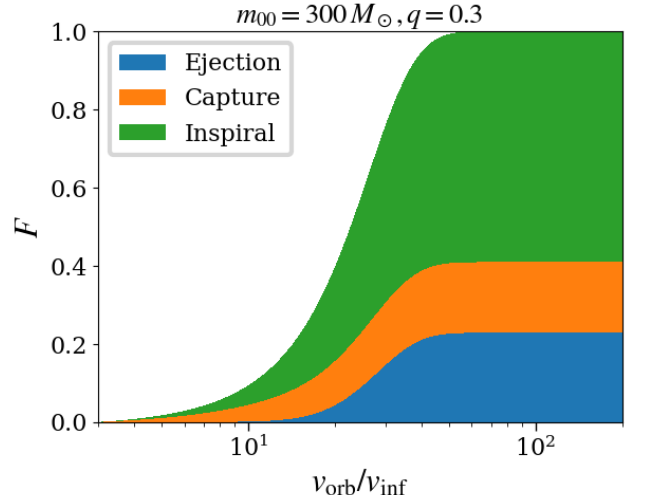


Figure 8. Stacked cumulative incidence functions for $m_{00} = 300 M_{\odot}$, $q = 0.3$, $v_{\text{inf}} = 20 \text{ km/s}$, and $n = 10^6 \text{ pc}^{-3}$. Here, the velocity acts as a time-like variable for a typical cumulative density function. The relative height of each colored region corresponds to the probability of the given outcome happening before the given binary hardness, such that when the three functions sum to 1 all binaries have either merged or have been dynamically ejected. The different colors correspond to ejection (blue, 23%), capture (orange, 18%), and inspiral (green, 59%), respectively.

merges between successive encounters, then the other two outcomes become forbidden by definition. This, among other considerations, motivates the use of semi-analytic codes to calculate outcome probabilities. However, under suitable simplifications, this problem can be cast in fully analytic terms using the fits from previous sections.

In this section, we use the numerical results of the previous section, as well as the methods of competing risk analysis described in Appendix B, to construct hazard functions and determine the distribution of outcomes for IMBH binaries with different parameters. We can construct the cause-specific hazard function for cause C with a given set of parameters $\theta = (m_{00}, q, v_{\text{inf}}, n)$:

$$h_C(v_{\text{orb}}|\theta) = \Sigma_C(v'_{\text{orb}}|\theta) \left| \frac{dE_0}{dt} \right|^{-1} \frac{dE_0}{dv'_{\text{orb}}}. \quad (24)$$

As v_{orb} becomes a time-like variable, the Jacobian-like additional factors are required since v_{orb} does not evolve linearly. We have made the approximation that the hardening rate $\frac{dE_0}{dt} \approx E_0 \Delta_a / T_{\text{enc}}$. Use of the Newtonian Δ_a found in Section 3.3 is valid when PN effects during interactions are subdominant, which is generally the case when $T_{\text{enc}} < T_{\text{GW}}$.

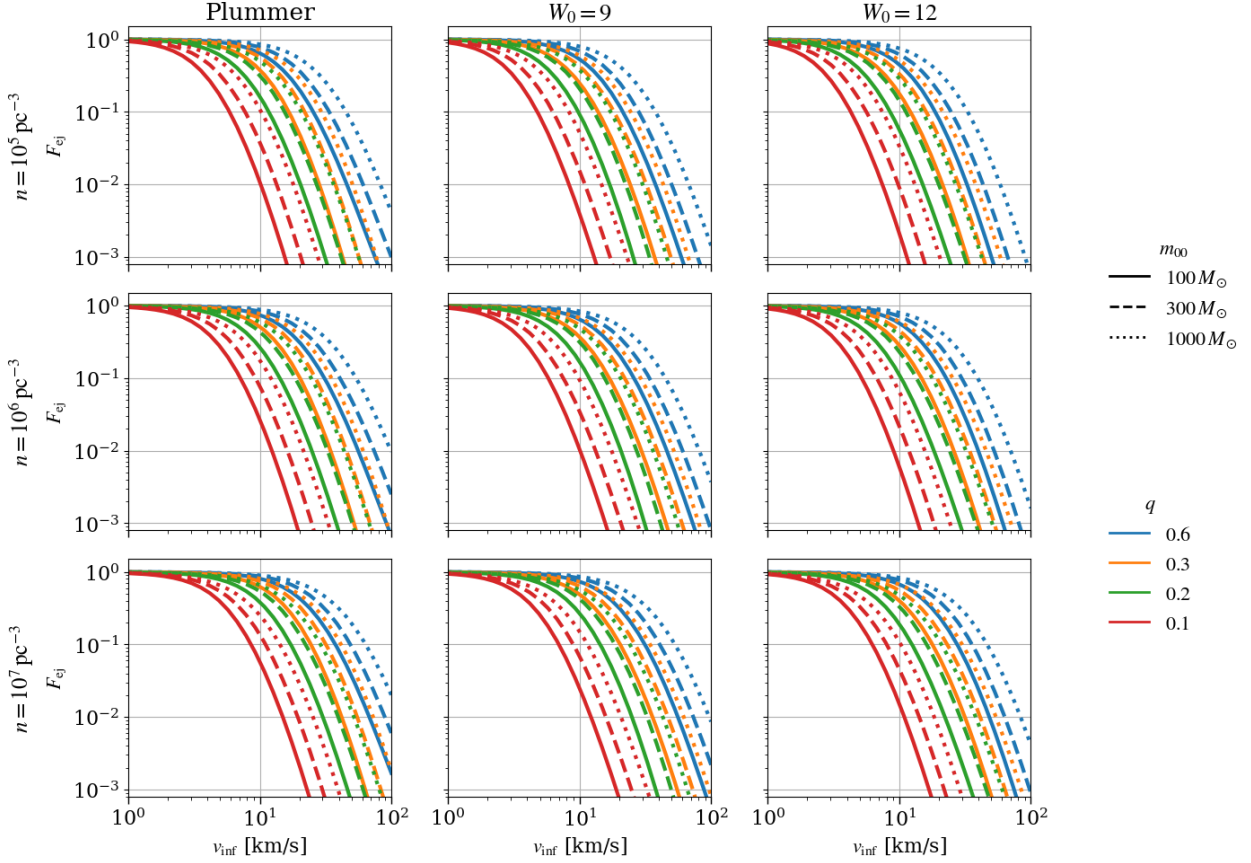


Figure 9. Maximum value of F_{ej} as a function of v_{inf} for different combinations of parameters. Each column represents a different assumed potential, with the most optimistic Plummer potential on the left and the most conservative $W_0 = 12$ King profile on the right. The rows increase in number density from top to bottom from 10^5 to 10^7 pc^{-3} . Blue, orange, green and red lines correspond to $q = 0.6, 0.3, 0.2,$ and 0.1 , respectively. Solid, dashed, and dotted lines correspond to $m_{00} = 100 M_{\odot}, 300 M_{\odot},$ and $1000 M_{\odot}$, respectively.

For the purposes of this calculation, we define three cause-specific hazards:

$$h_{ej} = \Sigma_{ej}(v'_{\text{orb}}|\theta) \left| \frac{dE_0}{dt} \right|^{-1} \frac{dE_0}{dv'_{\text{orb}}} \quad (25)$$

$$h_{\text{cap}} = \Sigma_{\text{cap}}(v'_{\text{orb}}|\theta) \left| \frac{dE_0}{dt} \right|^{-1} \frac{dE_0}{dv'_{\text{orb}}} \quad (26)$$

$$h_{\text{insp}} = \Sigma_{\text{insp}}(v'_{\text{orb}}|\theta) \left| \frac{dE_0}{dt} \right|^{-1} \frac{dE_0}{dv'_{\text{orb}}}. \quad (27)$$

Here we distinguish between binaries which merge between interactions, referred to as *inspirals*, and binaries which merge during interactions, referred to as *captures* as before. For the first two, we compute the rate using the Newtonian P_{ej} (Eq. 17) and post-Newtonian P_{cap} (Eq. 22) fits described above. We are justified in using the Newtonian form of P_{ej} because we find the post-Newtonian corrections are only significant when $T_{\text{enc}} > T_{\text{GW}}$ for all θ considered. For the third, we must construct the rate by hand since it does not follow from scattering experiments. After a given binary–

single interaction, all binaries will have a new eccentricity drawn from a thermal distribution. Some fraction f_{insp} will have a lifetime shorter than the mean time between encounters, which we compute by finding e_0 such that $T_{\text{enc}}/T_{\text{GW}} = 1$ and integrating over the thermal distribution. We take f_{insp} as P_{insp} to compute Σ_{insp} .

Then, we sum the cause-specific hazards to find the total hazard $h(v_{\text{orb}}|\theta)$ (Eq. B3) and integrate to obtain the survival function (Eq. B2),

$$S(v_{\text{orb}}|\theta) = \exp \left[- \int_{v_{\text{min}}}^{v_{\text{orb}}} dv'_{\text{orb}} h(v_{\text{orb}}|\theta) \right]. \quad (28)$$

From this the cause-specific incidence functions F_C follow from Eq. (B5):

$$F_C(v_{\text{orb}}|\theta) = \exp \left[- \int_{v_{\text{min}}}^{v_{\text{orb}}} dv'_{\text{orb}} h_C(v_{\text{orb}}|\theta) S(v_{\text{orb}}|\theta) \right]. \quad (29)$$

We show an example outcome of this calculation in Figure 8. In this example, we consider a $300 M_{\odot}$ IMBH encountering a population of $90 M_{\odot}$ BHs with $v_{\text{inf}} = 20$

km/s and $n = 10^6 \text{ pc}^{-3}$. We compute F_C for the three different outcomes and stack the results to find the total cumulative distribution function F . For convenience, we fill in the space below each line to correspond to the total probability of each outcome, with blue, orange, and green corresponding to ejection, capture, and inspiral, respectively. The x-axis is a time-like variable, in this case the hardness, so that the value of each F_C corresponds to the given outcomes occurring before that point in time. Here, the binaries have all been terminated by one of the three mechanisms by roughly $v_{\text{orb}}/v_{\text{inf}} = 60$, at which point all three curves plateau at their maximum value, which represents the integrated probability of the given outcome. Here, we can see that the majority of binaries (59%) terminate through inspiral, followed by those which are dynamically ejected (23%) and those merge via capture during interactions (18%). Binaries which are ejected are mostly ejected between $v_{\text{orb}}/v_{\text{inf}} = 20$ and $v_{\text{orb}}/v_{\text{inf}} = 40$.

In Figure 9, we show F_{ej} as a function of v_{inf} for different assumed parameters. The blue, orange, green, and red lines correspond to $q = 0.6, 0.3, 0.2, 0.1$ models, and the different line styles correspond to $m_{00} = 100 M_{\odot}$ (solid), $m_{00} = 300 M_{\odot}$ (dashed), and $m_{00} = 1000 M_{\odot}$ (dotted). The columns each assume a different potential and the rows a different central n . The range of v_{inf} chosen roughly corresponds to observed v_{esc} for GCs and nuclear star clusters (Antonini & Rasio 2016). We find that as v_{inf} grows (equivalently, as the cluster mass grows), the fraction of binaries which are dynamically ejected goes down, in agreement with expectations from scaling arguments (Eq. 23) and Monte Carlo simulations (e.g., Mai et al. 2025). F_{ej} is roughly unity at low v_{inf} but quickly transitions to a power-law, with the start of the transition depending on the assumed parameters. The largest effect comes from changing q , so that it is much harder to eject binaries at low q . For example, in the top left panel (Plummer, $n = 10^5 \text{ pc}^{-3}$), at $v_{\text{inf}} = 10$ km/s, the probability of ejecting a $100 M_{\odot}$ BH is roughly 20% for $q = 0.2$, but falls to 1% for $q = 0.1$. Changes in the other parameters result in more modest changes. For example, increasing the mass by a factor of 10 corresponds to a similar increase in ejection probability in the power law region of the function. Increasing n by a factor of 10 results in about a factor of 3 increase in ejection probability, as this increases the rate of interactions and decreases the window for an isolated inspiral. This weak dependence on m_{00} and n arise from the similarly weak dependence of T_{GW} on these parameters. Changing the assumed potential has the smallest effect on the probability. Thus, we can conclude that, for the mass ratios

shown, dynamical ejection is the most likely outcome at very low $v_{\text{inf}} \sim 1$ km/s. At intermediate v_{inf} , IMBHs may avoid dynamical ejection as long as they are sufficiently larger than the other BHs in the cluster. At high v_{inf} , dynamical ejection becomes essentially impossible, as expected.

4. DISCUSSION

4.1. Gravitational-wave Recoil

The final ingredient in our model is gravitational-wave recoil from the merger of two BHs. It is simple to incorporate in our model since the magnitude of the recoil kick v_{gw} depends on only three dimensionless quantities, q, χ_1, χ_2 , as well as the relative orientations of the BH spins. The magnitude of v_{gw} as a function of χ_1 and χ_2 , computed from fits to numerical relativity simulations (Campanelli et al. 2007; Lousto & Zlochower 2008; Lousto et al. 2010, 2012), is shown in Figure 10.

Previous studies found that these kicks eject the merger products except in the most massive clusters when the natal spin is sufficiently high ($\chi \gtrsim 0.5$) (e.g., Antonini & Rasio 2016; Fragione & Loeb 2021). However, if BHs born from stellar collapse have a negligible natal spin (Fuller & Ma 2019), then v_{gw} only depends on q , which corresponds to the blue curve in the leftmost panel. In this case, the maximum value of $v_{\text{gw}} \approx 175$ km/s occurs for $q \approx 0.35$, which is high enough to eject merger products from the most massive MW GCs. However, the assumption of negligible natal spin should be taken as the most optimistic estimate. Remnants of BBH mergers will be born with some spin due to angular momentum conservation. For example, for a merger between two roughly equal-mass BHs, the spin of the remnant is about $\chi = 0.7$. Moreover, it is possible for BHs to be spun up through accretion following collisions with stars (Kiroğlu et al. 2025a,c,b). In principle, this means that IMBHs which escape dynamical ejection are still at risk from being ejected by recoil kicks even in the most massive clusters, though this is also a strong function of q .

4.2. Other Escape Mechanisms

We have reviewed the two dominant mechanisms for ejection of IMBHs. However, there are other ways by which objects may escape clusters. All the potential escape mechanisms were studied in detail by Weatherford et al. (2023), which we summarize below to discuss the implications for our model.

Escape from clusters can be divided into two categories. The first, evaporation, is characterized by processes governed by the bulk evolution of the cluster on timescales much longer than the dynamical time. For

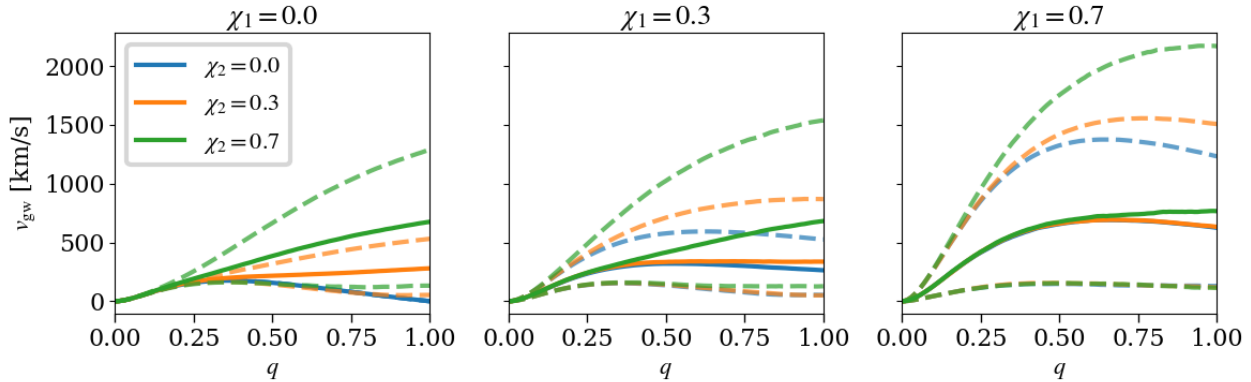


Figure 10. Magnitude of v_{gw} as a function of q for different combinations of spin for the primary and secondary. In order to produce the curves shown, we randomize the orientation of both spin vectors isotropically with respect to an arbitrary reference plane 4000 times for each set of curves and compute the resulting v_{gw} magnitude using fits to numerical relativity simulations (Campanelli et al. 2007; González et al. 2007; Lousto & Zlochower 2008; Lousto et al. 2012; Lousto & Zlochower 2013). The solid lines show the median recoil magnitude and the dashed lines show the 90% region. From left to right, we set χ_1 to 0, 0.3, and 0.7 in the different panels. Within each panel, we set the spin of χ_2 to 0 (blue), 0.3 (orange), and 0.7 (green), respectively.

example, individual objects may diffuse via 2-body relaxation to speeds above v_{esc} , which steadily decreases as the cluster loses mass through both dynamical mechanisms and stellar evolution. Furthermore, the strength of the tidal potential changes as the cluster orbits within the host galactic potential, thus potentially lowering the threshold for escaping. These evaporative processes are not expected to play a significant role in the fate of IMBHs, as these processes are most relevant for objects outside the cluster core. Dynamical friction, on the other hand, causes the orbits of heavy objects of mass M to decay into the center of the cluster on a timescale $t_{\text{df}} = \langle m \rangle t_{\text{relx}}$, where $\langle m \rangle$ is the average stellar mass and t_{relx} the relaxation time. For a typical cluster, $t_{\text{df}} \sim 1$ Myr. Additionally, an object that is only marginally unbound can take many relaxation timescales to actually escape, during which time the object can be scattered back into a lower-energy orbit. While it is possible that IMBH binaries which we considered marginally bound in our scattering experiments could escape through evaporative mechanisms, this correction is small and only relevant for low $v_{\text{orb}}/v_{\text{inf}}$ when escape is already so unlikely as to be negligible. Thus, it is unlikely that this would have a noticeable effect on F_{ej} calculated in Fig. 9.

On the other hand, ejection is expected to dominate in the core of the cluster, which was the environment we considered in this work. Escape by ejection is characterized by single, impulsive events that impart a recoil on objects greater than v_{esc} . This includes natal supernova kicks, strong gravitational interactions, and collision-induced recoil kicks. Strong gravitational interactions include, in addition to the binary–single interactions studied here, strong 2- and 3-body encounters between unbound singles and higher order few-body en-

counters. By construction, we have neglected supernova kicks in our model by assuming the presence of a population of BHs. BH natal kicks are highly uncertain; while observations of BH X-ray binaries suggest some BHs receive natal kicks as high as 100 km/s, many may receive kicks that are much lower (Repetto et al. 2017). Moreover, the observational and theoretical support for large populations of BHs in MW GCs support low natal kicks (e.g., Weatherford et al. 2020). We similarly neglect the effects of 2-body and 3-body encounters between singles as IMBHs are expected to efficiently exchange into binaries (e.g., Sigurdsson & Phinney 1993; Heggie et al. 1996). Moreover, while Weatherford et al. (2023) found that 3-body binary formation dominated the rate of high speed escapers, these were typically small single stars encountering much larger objects. Indeed, Atallah et al. (2024) found that binaries containing BHs formed via 3-body encounters rarely have a recoil above the v_{esc} assumed in our models. Similar reason holds for strong 2-body encounters; typically, an IMBH will impart a large kick onto a much smaller object, but the reverse is energetically not possible.

However, we must justify our suppression of binary–binary and higher order few-body encounters. The density of binaries is suppressed as soft BBHs tend to be ionized by the few (or single) harder BBH through direct ionization, triple formation, or gravitational-wave capture during a resonant interaction (Marín Pina & Gieles 2024; Marín Pina et al. 2025). Higher-order multiple systems are similarly expected to be quickly ionized in dense environments. Moreover, while the additional binding energy of the second binary can, in principle, result in higher v_{kick} compared to a single object of the same mass, the energy budget of the interaction will still

be dominated by the harder and more massive IMBH binary. Thus, we would not expect that the presence of a small number of BBHs to significantly affect either the rate of hardening or the rate of ejections. Indeed, [Weatherford et al. \(2023\)](#) reports that while the binary–binary mechanism results in a marginally higher median recoil speed, the rate of ejections is dominated by the binary–single mechanism.

In principle, it is possible that this assumption causes us to underpredict the number of mergers during interactions, as it has been shown that binary–binary interactions are responsible for a very large fraction of captures in the equal–mass case ([Zevin et al. 2019](#)). Similarly, secular evolution in triples formed by binary–binary interactions may also contribute to the merger rate, though the rate is very small compared to the total ([Martinez et al. 2020](#)). This may be important when considering the role of gravitational-wave recoil in ejecting IMBHs, even if this channel constitutes only a fraction of the total merger rate. Nevertheless, work in progress is underway studying the role of binary–binary encounters at early times involving two or more IMBHs ([Zhou et al., in prep.](#)).

4.3. Applications for Realistic Stellar Systems

The model presented in the previous section is highly idealized in comparison to realistic dense stellar environments. First, in realistic stellar systems, the mass distribution for BHs arises from a stellar IMF which is subsequently modified by collisions during dynamical interactions before the massive stars collapse into BHs. Second, σ_{disp} is not static, as is assumed in our model, but decreases from its initial value over time as the cluster loses mass through dynamical processes, so that it becomes easier to eject IMBHs over time. Nevertheless, it is expected that the largest BHs that form in a dense stellar environment will begin encountering each other due to mass segregation on timescales much faster than a relaxation time (within the first Gyr; see, e.g., [González Prieto et al. 2022](#)). Therefore, the fate of IMBHs formed in these environments depends on the initial σ_{disp} and v_{esc} and on the initial masses of the most massive BHs.

Previous work using N -body modeling studying the formation of IMBHs in dense stellar environments has shown that their formation is strongly dependent on highly uncertain initial conditions. Systematic exploration of initial conditions with both Monte Carlo simulations ([González et al. 2021](#); [Weatherford et al. 2021](#); [González Prieto et al. 2022, 2024](#); [Sharma & Rodriguez 2025](#); [Khurana & Chatterjee 2025](#)) and direct N -body methods ([Rantala et al. 2024](#); [Fujii et al. 2024](#); [Vergara et al. 2025](#); [Rantala et al. 2025, 2026](#)) have shown that

the formation of VMS progenitors of IMBHs, is strongly dependent on both the initial density of massive stars and the assumed stellar metallicity. A larger density of massive stars promotes a higher rate of stellar collisions prior to BH formation, while low metallicities are required such that stellar winds do not significantly erode the resulting hydrogen envelope. In these studies, it is shown that the largest IMBHs formed from direct collapse can be in the range of 10^2 to a few $10^4 M_{\odot}$ depending on initial conditions. When runaway collisions in extremely dense environments result in the production of a single large VMS, the resulting IMBH with $M \gtrsim 10^3 M_{\odot}$, formed from direct collapse reduces the number of BHs through the merger of massive star progenitors ([Sharma & Rodriguez 2025](#)). On the other hand, in simulations where the largest IMBH is only a few $10^2 M_{\odot}$, many IMBHs of similar mass and mass gap BHs may form, making retention unlikely in all but the most massive clusters ([González Prieto et al. 2022](#)).

While the initial properties of dense stellar clusters—such as the IMF, binary fractions, and cluster sizes—remain highly uncertain, JWST is starting to reveal the properties of young massive clusters (YMCs) at high redshifts. At redshift $z \sim 6$, NIRCAM imaging reveals YMCs with masses roughly $10^{6-7} M_{\odot}$ ([Vanzella et al. 2022](#)). In the Cosmic Gems Arc, five new proto-GC candidates have been found that exhibit stellar surface densities three orders of magnitude higher than young star clusters in the local universe ([Adamo et al. 2024](#)). Similar observations of stellar populations were recently reported in the Cosmic Spear ([Abdurro'uf et al. 2025](#)). More observational and theoretical work is necessary to constrain the initial properties of dense stellar environments in order to connect the clusters observed at these early times to those observed in the present and thus constrain the likelihood of IMBH formation.

4.4. Implications for IMBH candidates in the MW GCs

While direct detections of IMBHs in GCs remain elusive, several clues of their presence have begun to emerge. [Häberle et al. \(2024\)](#) report the detection of seven fast-moving stars, each exceeding the local inferred escape velocity, at the center of Omega Centauri. Alternative explanations for these high velocities, including foreground objects or tight binaries around a stellar mass BH, have been ruled out. Their findings therefore strongly suggest the presence of an IMBH with a mass in the range $8,200 - 50,000 M_{\odot}$ in Omega Centauri, which is theorized to be the stripped nucleus of a dwarf galaxy. Recently, CMC simulations—incorporating the relevant loss-cone physics for a fixed

central IMBH—have modeled the growth of the central IMBH and reproduced observed velocity and brightness profiles (González Prieto et al. 2025). González Prieto et al. (2025) found that models were most consistent with the observed properties of Omega Centauri when the simulation initial conditions included a truncation of the high end of the stellar IMF. This happens to be consistent with seed formation from runaway stellar collisions such that only one IMBH (the fixed potential) is initially formed such that it is immune to ejection by the stellar BHs that later form from stellar collapse.

Another cluster of interest is 47 Tucanae, where Paduano et al. (2024) identified a compact central radio source. Though the presence of a weakly accreting IMBH with a mass in the range $54 - 6000 M_{\odot}$ can be invoked, an undiscovered millisecond pulsar can't be ruled out. Furthermore, dynamical modeling by Della Croce et al. (2024) demonstrates that the observed stellar kinematics of the cluster's central region are incompatible with central IMBH masses greater than $578 M_{\odot}$. This more stringent upper limit on the mass is incompatible with our results. Ye et al. (2022) showed that the present-day observational properties of 47 Tucanae are well matched by a model containing a $\sim 2000 M_{\odot}$ BH subcluster and present day $\sigma_{\text{disp}} \simeq 15 \text{ km/s}$ without requiring the presence of an IMBH. The best-fit model presented there has an initial number of BHs roughly a factor of a few times higher than the present, corresponding to a similar factor increase in the total BH mass, and $\sigma_{\text{disp}} \simeq 30 - 40 \text{ km/s}$. While ejection at early times can be avoided by assuming that no IMBHs of comparable mass (say, $q \gtrsim 0.2 - 0.3$) were simultaneously formed, a $600 M_{\odot}$ IMBH would need to be roughly 10 times larger than the next most massive BHs to avoid ejection at times closer to the present. This is in tension with expectations from simulations. Furthermore, even a modest amount of spin would make such an IMBH liable to ejection from the cluster, even with $q \simeq 0.1$.

4.5. Gravitational Wave Observations

Though it may be unlikely to detect low-mass IMBHs through direct observations in the MW GCs, the low-mass IMBHs that are ejected in binaries through dynamics are still promising as potential multiband gravitational-wave sources with current and future gravitational wave detectors such as LISA, Cosmic Explorer, and the Einstein Telescope (see Jani et al. 2020, for a detailed discussion). Detailed rate estimates for different instruments are outside the scope of this work, but we can make qualitative comments in the context of our results.

Analysis of the population properties of GWTC-4 data has shown that the differential merger rate for the underlying astrophysical population is consistent with a power law with index $\beta_q = 1.2_{-1.0}^{+1.2}$, so that mergers with $q \simeq 1$ are 1000 times more common than mergers with $q \simeq 0.1$ (The LIGO Scientific Collaboration et al. 2025). Our results suggest that, since IMBHs with comparable masses are more likely to be ejected, they will tend to merge at redshifts near $z = 0$, which is consistent with the reported astrophysical population properties. On the other hand, IMBH binaries with large mass asymmetry tend to merge within their host cluster, such that these mergers are more likely to happen at early times. Thus, it is possible that IMBH mergers with $q \lesssim 0.2$ may be more common at higher redshift. This is especially true if some of these IMBHs are retained following the merger, as they will merge efficiently with stellar-mass BHs (González Prieto et al. 2025).

5. SUMMARY

We have studied the relative importance of dynamical recoil and gravitational-wave recoil for ejecting IMBHs from star clusters. For this end, we have presented the results of both Newtonian and post-Newtonian scattering experiments of intermediate mass ratios. From our scattering experiments, we provided fits to the branching ratios for ejection P_{ej} and gravitational-wave capture P_{cap} , as well as the per-encounter hardening rate $\langle \Delta \rangle$ for binary–single interactions where $m_{00} > m_{01} = m_1$ for $q = 0.01 - 0.6$. Using these fits, we created a toy model for IMBH binary evolution in dense stellar environments and use methods borrowed from survival analysis to compute the probability of ejection for an IMBH-BH binary through dynamical interactions. We find that the probability of ejection for a given IMBH binary is most sensitive to the cluster velocity dispersion (σ_{disp}) and the mass ratio of the IMBH with respect to other BHs in the cluster, with dynamical ejection being dominant at low σ_{disp} and improbable for high σ_{disp} . However, IMBHs which are immune to dynamical ejection may still be at risk for ejection by gravitational wave recoil depending on assumption about the natal spin. We discuss the implications of our toy model for observations of IMBHs and find that, while direct detection of IMBHs with masses of order $10^2 M_{\odot}$ is unlikely in present-day clusters, it is possible that future gravitational wave detectors might detect the merger of IMBH binaries in this mass range with asymmetric mass ratios.

6. ACKNOWLEDGMENTS

We thank Christopher O'Connor, Sanaea Rose, Dany Atallah, Giacomo Fragione, Yonadav Barry Ginat,

Nicholas Stone, Aaron Tierney, and Emiko Kranz for helpful discussions and comments. This work was supported by NSF Grants AST-2108624 and AST-2511543 at CIERA, and used computing resources funded by NSF Grants PHY-1726951 and PHY-2406802. Our research was supported in part through the computational resources and staff contributions provided for the Quest high performance computing facility at Northwestern

University, which is jointly supported by the Office of the Provost, the Office for Research, and Northwestern University Information Technology. Support for E.G.P. was provided by the NSF Graduate Research Fellowship Program under Grant DGE-2234667.

Software: Fewbody (Fregeau et al. 2004), NumPy (Harris et al. 2020), SciPy (Virtanen et al. 2020), pandas (Wes McKinney 2010; pandas development team 2020), Matplotlib (Hunter 2007)

REFERENCES

- Aalen, O. O., Borgan, O., & Gjessing, H. K. 2008, Survival and Event History Analysis: A Process Point of View, Statistics for Biology and Health (Springer)
- Abac, A. G., Abouelfettouh, I., Acernese, F., et al. 2025, ApJL, 993, L25, doi: [10.3847/2041-8213/ae0c9c](https://doi.org/10.3847/2041-8213/ae0c9c)
- Abdurro'uf, Coe, D., Resseguier, T., et al. 2025, arXiv e-prints, arXiv:2512.08054.
<https://arxiv.org/abs/2512.08054>
- Adamo, A., Bradley, L. D., Vanzella, E., et al. 2024, Nature, 632, 513, doi: [10.1038/s41586-024-07703-7](https://doi.org/10.1038/s41586-024-07703-7)
- Antonini, F., Gieles, M., & Gualandris, A. 2019, MNRAS, 486, 5008, doi: [10.1093/mnras/stz1149](https://doi.org/10.1093/mnras/stz1149)
- Antonini, F., & Rasio, F. A. 2016, ApJ, 831, 187, doi: [10.3847/0004-637X/831/2/187](https://doi.org/10.3847/0004-637X/831/2/187)
- Atallah, D., Trani, A. A., Kremer, K., et al. 2023, MNRAS, 523, 4227, doi: [10.1093/mnras/stad1634](https://doi.org/10.1093/mnras/stad1634)
- Atallah, D., Weatherford, N. C., Trani, A. A., & Rasio, F. A. 2024, ApJ, 970, 112, doi: [10.3847/1538-4357/ad5185](https://doi.org/10.3847/1538-4357/ad5185)
- Bailyn, C. D. 1989, ApJ, 341, 175, doi: [10.1086/167482](https://doi.org/10.1086/167482)
- Ballone, A., Costa, G., Mapelli, M., et al. 2023, MNRAS, 519, 5191, doi: [10.1093/mnras/stac3752](https://doi.org/10.1093/mnras/stac3752)
- Banerjee, S. 2020, Monthly Notices of the Royal Astronomical Society, 500, 3002–3026, doi: [10.1093/mnras/staa2392](https://doi.org/10.1093/mnras/staa2392)
- Binney, J., & Tremaine, S. 2008, Galactic Dynamics: Second Edition (Princeton University Press)
- Boubert, D., Guillochon, J., Hawkins, K., et al. 2018, MNRAS, 479, 2789, doi: [10.1093/mnras/sty1601](https://doi.org/10.1093/mnras/sty1601)
- Breen, P. G., & Hogg, D. C. 2013, MNRAS, 432, 2779, doi: [10.1093/mnras/stt628](https://doi.org/10.1093/mnras/stt628)
- Brown, W. R., Geller, M. J., Kenyon, S. J., & Kurtz, M. J. 2005, ApJL, 622, L33, doi: [10.1086/429378](https://doi.org/10.1086/429378)
- Campanelli, M., Lousto, C., Zlochower, Y., & Merritt, D. 2007, ApJL, 659, L5, doi: [10.1086/516712](https://doi.org/10.1086/516712)
- Chattopadhyay, D., Stegmann, J., Antonini, F., Barber, J., & Romero-Shaw, I. M. 2023, MNRAS, 526, 4908, doi: [10.1093/mnras/stad3048](https://doi.org/10.1093/mnras/stad3048)
- Chazy, J. 1929, Journal de mathematiques pures et appliquees, 8, 353
- Chen, J.-H., & Shen, R.-F. 2018, ApJ, 867, 20, doi: [10.3847/1538-4357/aadfa](https://doi.org/10.3847/1538-4357/aadfa)
- Chen, S., Hare, J., Kargaltsev, O., et al. 2025, arXiv e-prints, arXiv:2511.20945, doi: [10.48550/arXiv.2511.20945](https://doi.org/10.48550/arXiv.2511.20945)
- Costa, G., Ballone, A., Mapelli, M., & Bressan, A. 2022, MNRAS, 516, 1072, doi: [10.1093/mnras/stac2222](https://doi.org/10.1093/mnras/stac2222)
- Dejonghe, H. 1987, MNRAS, 224, 13, doi: [10.1093/mnras/224.1.13](https://doi.org/10.1093/mnras/224.1.13)
- Della Croce, A., Pascale, R., Giunchi, E., et al. 2024, A&A, 682, A22, doi: [10.1051/0004-6361/202347569](https://doi.org/10.1051/0004-6361/202347569)
- Di Carlo, U. N., Giacobbo, N., Mapelli, M., et al. 2019, MNRAS, 487, 2947, doi: [10.1093/mnras/stz1453](https://doi.org/10.1093/mnras/stz1453)
- Fragione, G., Kocsis, B., Rasio, F. A., & Silk, J. 2022, ApJ, 927, 231, doi: [10.3847/1538-4357/ac5026](https://doi.org/10.3847/1538-4357/ac5026)
- Fragione, G., & Loeb, A. 2021, MNRAS, 502, 3879, doi: [10.1093/mnras/stab247](https://doi.org/10.1093/mnras/stab247)
- Fragione, G., Loeb, A., & Rasio, F. A. 2020, ApJL, 902, L26, doi: [10.3847/2041-8213/abbc0a](https://doi.org/10.3847/2041-8213/abbc0a)
- Fragione, G., & Silk, J. 2020, MNRAS, 498, 4591, doi: [10.1093/mnras/staa2629](https://doi.org/10.1093/mnras/staa2629)
- Fregeau, J. M., Cheung, P., Portegies Zwart, S. F., & Rasio, F. A. 2004, MNRAS, 352, 1, doi: [10.1111/j.1365-2966.2004.07914.x](https://doi.org/10.1111/j.1365-2966.2004.07914.x)
- Fujii, M. S., Wang, L., Tanikawa, A., Hirai, Y., & Saitoh, T. R. 2024, Science, 384, 1488, doi: [10.1126/science.adi4211](https://doi.org/10.1126/science.adi4211)
- Fuller, J., & Ma, L. 2019, ApJL, 881, L1, doi: [10.3847/2041-8213/ab339b](https://doi.org/10.3847/2041-8213/ab339b)
- Gerosa, D., & Berti, E. 2019, PhRvD, 100, 041301, doi: [10.1103/PhysRevD.100.041301](https://doi.org/10.1103/PhysRevD.100.041301)
- Ginat, Y. B., & Perets, H. B. 2021, MNRAS, 508, 190, doi: [10.1093/mnras/stab2565](https://doi.org/10.1093/mnras/stab2565)
- González, E., Kremer, K., Chatterjee, S., et al. 2021, ApJL, 908, L29, doi: [10.3847/2041-8213/abd5b](https://doi.org/10.3847/2041-8213/abd5b)

- González, J. A., Spherhake, U., Brüggmann, B., Hannam, M., & Husa, S. 2007, *PhRvL*, 98, 091101, doi: [10.1103/PhysRevLett.98.091101](https://doi.org/10.1103/PhysRevLett.98.091101)
- González Prieto, E., Kremer, K., Fragione, G., et al. 2022, *ApJ*, 940, 131, doi: [10.3847/1538-4357/ac9b0f](https://doi.org/10.3847/1538-4357/ac9b0f)
- González Prieto, E., Rodríguez, C. L., & Cabrera, T. 2025, *ApJL*, 990, L69, doi: [10.3847/2041-8213/adfd4a](https://doi.org/10.3847/2041-8213/adfd4a)
- González Prieto, E., Weatherford, N. C., Fragione, G., Kremer, K., & Rasio, F. A. 2024, *ApJ*, 969, 29, doi: [10.3847/1538-4357/ad43d6](https://doi.org/10.3847/1538-4357/ad43d6)
- Greene, J. E., Strader, J., & Ho, L. C. 2020, *ARA&A*, 58, 257, doi: [10.1146/annurev-astro-032620-021835](https://doi.org/10.1146/annurev-astro-032620-021835)
- Haas, R., Shcherbakov, R. V., Bode, T., & Laguna, P. 2012, *ApJ*, 749, 117, doi: [10.1088/0004-637X/749/2/117](https://doi.org/10.1088/0004-637X/749/2/117)
- Häberle, M., Neumayer, N., Seth, A., et al. 2024, *Nature*, 631, 285, doi: [10.1038/s41586-024-07511-z](https://doi.org/10.1038/s41586-024-07511-z)
- Hansen, R. O. 1972, *PhRvD*, 5, 1021, doi: [10.1103/PhysRevD.5.1021](https://doi.org/10.1103/PhysRevD.5.1021)
- Harris, C. R., Millman, K. J., van der Walt, S. J., et al. 2020, *Nature*, 585, 357, doi: [10.1038/s41586-020-2649-2](https://doi.org/10.1038/s41586-020-2649-2)
- Harris, W. E. 1996, *AJ*, 112, 1487, doi: [10.1086/118116](https://doi.org/10.1086/118116)
- Hayashi, T., Trani, A. A., & Suto, Y. 2022, *ApJ*, 939, 81, doi: [10.3847/1538-4357/ac8f48](https://doi.org/10.3847/1538-4357/ac8f48)
- . 2023, *ApJ*, 943, 58, doi: [10.3847/1538-4357/acac1e](https://doi.org/10.3847/1538-4357/acac1e)
- Heggie, D. C. 1975, *MNRAS*, 173, 729, doi: [10.1093/mnras/173.3.729](https://doi.org/10.1093/mnras/173.3.729)
- Heggie, D. C., Hut, P., & McMillan, S. L. W. 1996, *ApJ*, 467, 359, doi: [10.1086/177611](https://doi.org/10.1086/177611)
- Hunter, J. D. 2007, *Computing in Science & Engineering*, 9, 90, doi: [10.1109/MCSE.2007.55](https://doi.org/10.1109/MCSE.2007.55)
- Hut, P., & Bahcall, J. N. 1983, *ApJ*, 268, 319, doi: [10.1086/160956](https://doi.org/10.1086/160956)
- Jani, K., Shoemaker, D., & Cutler, C. 2020, *Nature Astronomy*, 4, 260, doi: [10.1038/s41550-019-0932-7](https://doi.org/10.1038/s41550-019-0932-7)
- Jeans, J. H. 1919, *MNRAS*, 79, 408, doi: [10.1093/mnras/79.6.408](https://doi.org/10.1093/mnras/79.6.408)
- Khurana, A., & Chatterjee, S. 2025, *ApJ*, 986, 82, doi: [10.3847/1538-4357/add337](https://doi.org/10.3847/1538-4357/add337)
- King, I. 1962, *AJ*, 67, 471, doi: [10.1086/108756](https://doi.org/10.1086/108756)
- Kiroğlu, F., Kremer, K., Biscoveanu, S., González Prieto, E., & Rasio, F. A. 2025a, *ApJ*, 979, 237, doi: [10.3847/1538-4357/ada26b](https://doi.org/10.3847/1538-4357/ada26b)
- Kiroğlu, F., Kremer, K., & Rasio, F. A. 2025b, *ApJL*, 994, L37, doi: [10.3847/2041-8213/ae1eeb](https://doi.org/10.3847/2041-8213/ae1eeb)
- Kiroğlu, F., Lombardi, J. C., Kremer, K., et al. 2023, *ApJ*, 948, 89, doi: [10.3847/1538-4357/acc24c](https://doi.org/10.3847/1538-4357/acc24c)
- Kiroğlu, F., Lombardi, J. C., Kremer, K., Vanderzypden, H. D., & Rasio, F. A. 2025c, *ApJL*, 983, L9, doi: [10.3847/2041-8213/adc263](https://doi.org/10.3847/2041-8213/adc263)
- Koposov, S. E., Boubert, D., Li, T. S., et al. 2020, *MNRAS*, 491, 2465, doi: [10.1093/mnras/stz3081](https://doi.org/10.1093/mnras/stz3081)
- Kremer, K., Spera, M., Becker, D., et al. 2020a, arXiv e-prints, arXiv:2006.10771, <https://arxiv.org/abs/2006.10771>
- Kremer, K., Ye, C. S., Rui, N. Z., et al. 2020b, *ApJS*, 247, 48, doi: [10.3847/1538-4365/ab7919](https://doi.org/10.3847/1538-4365/ab7919)
- Kritos, K., Stokov, V., Baibhav, V., & Berti, E. 2024, *PhRvD*, 110, 043023, doi: [10.1103/PhysRevD.110.043023](https://doi.org/10.1103/PhysRevD.110.043023)
- Lalande, F., & Trani, A. A. 2022, *ApJ*, 938, 18, doi: [10.3847/1538-4357/ac8eab](https://doi.org/10.3847/1538-4357/ac8eab)
- Lousto, C. O., Campanelli, M., Zlochower, Y., & Nakano, H. 2010, *Classical and Quantum Gravity*, 27, 114006, doi: [10.1088/0264-9381/27/11/114006](https://doi.org/10.1088/0264-9381/27/11/114006)
- Lousto, C. O., & Zlochower, Y. 2008, *PhRvD*, 77, 044028, doi: [10.1103/PhysRevD.77.044028](https://doi.org/10.1103/PhysRevD.77.044028)
- . 2013, *PhRvD*, 87, 084027, doi: [10.1103/PhysRevD.87.084027](https://doi.org/10.1103/PhysRevD.87.084027)
- Lousto, C. O., Zlochower, Y., Dotti, M., & Volonteri, M. 2012, *PhRvD*, 85, 084015, doi: [10.1103/PhysRevD.85.084015](https://doi.org/10.1103/PhysRevD.85.084015)
- MacLeod, M., Guillochon, J., Ramirez-Ruiz, E., Kasen, D., & Rosswog, S. 2016, *ApJ*, 819, 3, doi: [10.3847/0004-637X/819/1/3](https://doi.org/10.3847/0004-637X/819/1/3)
- Mai, A., Kremer, K., & Kiroglu, F. 2025, arXiv e-prints, arXiv:2510.21916, doi: [10.48550/arXiv.2510.21916](https://doi.org/10.48550/arXiv.2510.21916)
- Manwadkar, V., Trani, A. A., & Leigh, N. W. C. 2020, *MNRAS*, 497, 3694, doi: [10.1093/mnras/staa1722](https://doi.org/10.1093/mnras/staa1722)
- Mardling, R. A., & Aarseth, S. J. 2001, *MNRAS*, 321, 398, doi: [10.1046/j.1365-8711.2001.03974.x](https://doi.org/10.1046/j.1365-8711.2001.03974.x)
- Marín Pina, D., & Gieles, M. 2024, *MNRAS*, 527, 8369, doi: [10.1093/mnras/stad3777](https://doi.org/10.1093/mnras/stad3777)
- Marín Pina, D., Gieles, M., Andrade, T., & Trani, A. A. 2025, *A&A*, 698, A229, doi: [10.1051/0004-6361/202453531](https://doi.org/10.1051/0004-6361/202453531)
- Martinez, M. A. S., Fragione, G., Kremer, K., et al. 2020, *ApJ*, 903, 67, doi: [10.3847/1538-4357/abba25](https://doi.org/10.3847/1538-4357/abba25)
- McKernan, B., Ford, K. E. S., Lyra, W., & Perets, H. B. 2012, *MNRAS*, 425, 460, doi: [10.1111/j.1365-2966.2012.21486.x](https://doi.org/10.1111/j.1365-2966.2012.21486.x)
- McMillan, S. L. W., & Hut, P. 1996, *ApJ*, 467, 348, doi: [10.1086/177610](https://doi.org/10.1086/177610)
- Miller, M. C., & Hamilton, D. P. 2002, *MNRAS*, 330, 232, doi: [10.1046/j.1365-8711.2002.05112.x](https://doi.org/10.1046/j.1365-8711.2002.05112.x)
- Paduano, A., Bahramian, A., Miller-Jones, J. C. A., et al. 2024, *ApJ*, 961, 54, doi: [10.3847/1538-4357/ad0e68](https://doi.org/10.3847/1538-4357/ad0e68)
- pandas development team, T. 2020, *pandas-dev/pandas: Pandas, latest*, Zenodo, doi: [10.5281/zenodo.3509134](https://doi.org/10.5281/zenodo.3509134)
- Peters, P. C. 1964, *Physical Review*, 136, 1224, doi: [10.1103/PhysRev.136.B1224](https://doi.org/10.1103/PhysRev.136.B1224)

- Plummer, H. C. 1911, *MNRAS*, 71, 460,
doi: [10.1093/mnras/71.5.460](https://doi.org/10.1093/mnras/71.5.460)
- Quinlan, G. D. 1996, *NewA*, 1, 35,
doi: [10.1016/S1384-1076\(96\)00003-6](https://doi.org/10.1016/S1384-1076(96)00003-6)
- Ramirez-Ruiz, E., & Rosswog, S. 2009, *ApJL*, 697, L77,
doi: [10.1088/0004-637X/697/2/L77](https://doi.org/10.1088/0004-637X/697/2/L77)
- Rando Forastier, B., Marín Pina, D., Gieles, M., Portegies Zwart, S., & Antonini, F. 2025, *A&A*, 697, A118,
doi: [10.1051/0004-6361/202450890](https://doi.org/10.1051/0004-6361/202450890)
- Rantala, A., Lahén, N., Naab, T., Escobar, G. J., & Iorio, G. 2025, *MNRAS*, 543, 2130,
doi: [10.1093/mnras/staf1519](https://doi.org/10.1093/mnras/staf1519)
- Rantala, A., Naab, T., & Lahén, N. 2024, *MNRAS*, 531, 3770, doi: [10.1093/mnras/stae1413](https://doi.org/10.1093/mnras/stae1413)
- Rantala, A., Naab, T., Lahén, N., et al. 2026, arXiv e-prints, arXiv:2601.07917.
<https://arxiv.org/abs/2601.07917>
- Rasskazov, A., Fragione, G., Leigh, N. W. C., et al. 2019, *ApJ*, 878, 17, doi: [10.3847/1538-4357/ab1c5d](https://doi.org/10.3847/1538-4357/ab1c5d)
- Repetto, S., Igoshev, A. P., & Nelemans, G. 2017, *MNRAS*, 467, 298, doi: [10.1093/mnras/stx027](https://doi.org/10.1093/mnras/stx027)
- Rizzuto, F. P., Naab, T., Rantala, A., et al. 2023, *MNRAS*, 521, 2930, doi: [10.1093/mnras/stad734](https://doi.org/10.1093/mnras/stad734)
- Rizzuto, F. P., Naab, T., Spurzem, R., et al. 2021, *MNRAS*, 501, 5257, doi: [10.1093/mnras/staa3634](https://doi.org/10.1093/mnras/staa3634)
- Rodriguez, C. L., Amaro-Seoane, P., Chatterjee, S., et al. 2018, *PhRvD*, 98, 123005,
doi: [10.1103/PhysRevD.98.123005](https://doi.org/10.1103/PhysRevD.98.123005)
- Rodriguez, C. L., Zevin, M., Amaro-Seoane, P., et al. 2019, *PhRvD*, 100, 043027, doi: [10.1103/PhysRevD.100.043027](https://doi.org/10.1103/PhysRevD.100.043027)
- Samsing, J. 2018, *PhRvD*, 97, 103014,
doi: [10.1103/PhysRevD.97.103014](https://doi.org/10.1103/PhysRevD.97.103014)
- Samsing, J., MacLeod, M., & Ramirez-Ruiz, E. 2014, *ApJ*, 784, 71, doi: [10.1088/0004-637X/784/1/71](https://doi.org/10.1088/0004-637X/784/1/71)
- Sesana, A., Haardt, F., & Madau, P. 2006, *ApJ*, 651, 392,
doi: [10.1086/507596](https://doi.org/10.1086/507596)
- Sharma, K., & Rodriguez, C. L. 2025, *ApJ*, 983, 162,
doi: [10.3847/1538-4357/adbbdf](https://doi.org/10.3847/1538-4357/adbbdf)
- Sigurdsson, S., & Phinney, E. S. 1993, *ApJ*, 415, 631,
doi: [10.1086/173190](https://doi.org/10.1086/173190)
- Spera, M., Mapelli, M., Giacobbo, N., et al. 2019, *MNRAS*, 485, 889, doi: [10.1093/mnras/stz359](https://doi.org/10.1093/mnras/stz359)
- The LIGO Scientific Collaboration, the Virgo Collaboration, the KAGRA Collaboration, et al. 2025, arXiv e-prints, arXiv:2508.18083,
doi: [10.48550/arXiv.2508.18083](https://doi.org/10.48550/arXiv.2508.18083)
- Trani, A. A., Leigh, N. W. C., Boehholt, T. C. N., & Portegies Zwart, S. 2024, *A&A*, 689, A24,
doi: [10.1051/0004-6361/202449862](https://doi.org/10.1051/0004-6361/202449862)
- Vanzella, E., Castellano, M., Bergamini, P., et al. 2022, *ApJL*, 940, L53, doi: [10.3847/2041-8213/ac8c2d](https://doi.org/10.3847/2041-8213/ac8c2d)
- Vergara, M. C., Askar, A., Flammini Dotti, F., et al. 2025, arXiv e-prints, arXiv:2508.14260,
doi: [10.48550/arXiv.2508.14260](https://doi.org/10.48550/arXiv.2508.14260)
- Virtanen, P., Gommers, R., Oliphant, T. E., et al. 2020, *Nature Methods*, 17, 261, doi: [10.1038/s41592-019-0686-2](https://doi.org/10.1038/s41592-019-0686-2)
- Weatherford, N. C., Chatterjee, S., Kremer, K., & Rasio, F. A. 2020, *ApJ*, 898, 162, doi: [10.3847/1538-4357/ab9f98](https://doi.org/10.3847/1538-4357/ab9f98)
- Weatherford, N. C., Fragione, G., Kremer, K., et al. 2021, *ApJL*, 907, L25, doi: [10.3847/2041-8213/abd79c](https://doi.org/10.3847/2041-8213/abd79c)
- Weatherford, N. C., Kiroğlu, F., Fragione, G., et al. 2023, *ApJ*, 946, 104, doi: [10.3847/1538-4357/acbcc1](https://doi.org/10.3847/1538-4357/acbcc1)
- Wes McKinney. 2010, in *Proceedings of the 9th Python in Science Conference*, ed. Stéfan van der Walt & Jarrod Millman, 56 – 61, doi: [10.25080/Majora-92bf1922-00a](https://doi.org/10.25080/Majora-92bf1922-00a)
- Ye, C. S., Kremer, K., Rodriguez, C. L., et al. 2022, *ApJ*, 931, 84, doi: [10.3847/1538-4357/ac5b0b](https://doi.org/10.3847/1538-4357/ac5b0b)
- Zevin, M., Samsing, J., Rodriguez, C., Haster, C.-J., & Ramirez-Ruiz, E. 2019, *ApJ*, 871, 91,
doi: [10.3847/1538-4357/aaf6ec](https://doi.org/10.3847/1538-4357/aaf6ec)

APPENDIX

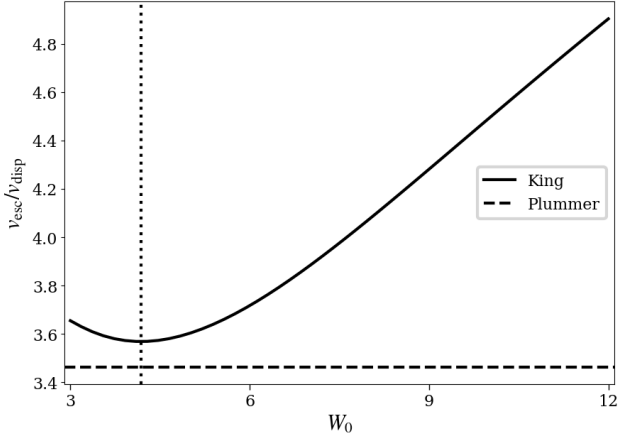


Figure 11. Ratio of escape speed from the center of the cluster to velocity dispersion for a King profile with different values of W_0 . The dashed black line showed the corresponding quantity for a Plummer profile.

A. CENTRAL ESCAPE SPEED IN KING PROFILE

The King profile is characterized by the distribution function

$$f(\mathcal{E}) = \rho_0 (2\pi\sigma^2)^{-3/2} (e^{\mathcal{E}/\sigma^2} - 1)$$

when the relative energy $\mathcal{E} = \Psi - v^2/2 > 0$ and is equal to 0 otherwise, $\Psi(r) = \Phi(r_t) - \Phi(r)$ is the relative potential, r_t is the tidal radius, and ρ_0 is the central density. Note that the parameter σ , which characterizes the thermal energy of the objects in the cluster, is closely related but not equivalent to the physical velocity dispersion σ_{disp} . Integrating the distribution function over all velocities, we find (e.g., [Binney & Tremaine 2008](#))

$$\rho(\Psi) = \rho_0 \left[e^{\Psi/\sigma^2} \operatorname{erf} \left(\sqrt{\frac{\Psi}{\sigma^2}} \right) - \sqrt{\frac{4\Psi}{\pi\sigma^2}} \left(1 + \frac{2\Psi}{3\sigma^2} \right) \right]$$

Now, from here, one may wish to find the functional form of the relative potential $\Psi(r)$, which would require integrating the equation of Poisson, which would allow one to find a functional form for $\rho(r)$. However, it is clear from the form of $\rho(\Psi)$ that the family of King models can be described by a single parameter $W_0 = \Psi(0)/\sigma^2$. This value sets the shape of the density–potential pair. Choosing a radial scale, such as the King (core) radius

$$r_c = \sqrt{\frac{9\sigma^2}{4\pi G\rho_0}}$$

sets the scale of the system. Finally, setting either a central density ρ_0 or a total cluster mass M_{tot} allows one to

find a dimensionful value of the parameter σ , which completely determines the parameters of the cluster model. The escape velocity from the cluster core is

$$v_{\text{esc}}(0) = \sqrt{2\Psi(0)} = \sqrt{2W_0}\sigma. \quad (\text{A1})$$

The velocity dispersion σ_{disp} can be found by integrating the appropriate moment of the distribution function ([Dejonghe 1987](#)):

$$\sigma^2(\Psi) = \frac{1}{\rho(\Psi)} \int_0^\Psi \rho(\Psi') d\Psi'.$$

Thus we find that σ_{disp} is related to σ by the relation

$$\begin{aligned} \sigma_{\text{disp}}^2(\Psi) = \sigma^2 & \left(e^{\Psi/\sigma^2} \operatorname{erf} \left(\sqrt{\frac{\Psi}{\sigma^2}} \right) - \frac{2}{\sqrt{\pi}} \left(\frac{\Psi}{\sigma^2} \right)^{1/2} \right. \\ & \left. - \frac{4}{3\sqrt{\pi}} \left(\frac{\Psi}{\sigma^2} \right)^{3/2} - \frac{8}{15\sqrt{\pi}} \left(\frac{\Psi}{\sigma^2} \right)^{5/2} \right) \\ & \left[e^{\Psi/\sigma^2} \operatorname{erf} \left(\sqrt{\frac{\Psi}{\sigma^2}} \right) - \sqrt{\frac{4\Psi}{\pi\sigma^2}} \left(1 + \frac{2\Psi}{3\sigma^2} \right) \right]^{-1} \end{aligned} \quad (\text{A2})$$

In [Figure 11](#), we show the ratio of the central values $v_{\text{esc}}/\sigma_{\text{disp}}$ as a function of W_0 (solid) for the King model compared to that for a Plummer model (dashed). The value of the ratio $v_{\text{esc}}/\sigma_{\text{disp}}$ for King models is higher than that of the Plummer profile within the range of interest by an order unity factor and is closest for $W_0 \approx 4.2$.

B. SURVIVAL ANALYSIS AND COMPETING RISK ANALYSIS

In this study, we make use of the results of survival analysis, which are used widely in other fields concerned with system failure, e.g. human mortality rates, failure of mechanical components, etc. In these fields, the below methods are standard and many references can be easily found, but we refer the reader to [Aalen et al. \(2008\)](#) for an extremely mathematically rigorous treatment of this subject.

The rate of ejections Σ_{ej} shares properties with what is called the hazard function $h(t)$, defined as

$$h(t) = \lim_{\Delta t \rightarrow 0} \frac{P(t \leq T < t + \Delta t \mid T \geq t)}{\Delta t}, \quad (\text{B1})$$

where T is the true failure time. This can be understood as the instantaneous rate of failure of a system at time

t given that the system has survived until t . By manipulating Eq. (B1), it can be shown that $h(t)$ is related to the probability distribution function of failure times $f(t)$ and the survival function $S(t) = 1 - F(t)$ by

$$h(t) = \frac{f(t)}{S(t)} = -\frac{d}{dt} \ln S(t). \quad (\text{B2})$$

The significance of these functions for our results is as follows: if we can construct $h(v_{\text{orb}})$ from Σ_{ej} , then $S(v_{\text{orb}})$ corresponds to the fraction of systems that have survived ejection at a given v_{orb} . Then, $f(v_{\text{orb}})$ corresponds to the distribution with which binaries are ejected, which can be transformed into, e.g., a delay time distribution of gravitational-wave merger events.

However, just as there are multiple competing causes of mortality, the binaries too have different end states. Thus, we need to use competing risk analysis, which generalizes the above for cause-specific hazard functions h_c . The total hazard is

$$h(t) = \sum_c h_c(t) \quad (\text{B3})$$

such that, if the intrinsic hazards are independent of each other, the incidence probability for a single failure mode is

$$I_c(t) = S(t)h_c(t). \quad (\text{B4})$$

Note that the incidence probability is *not* a probability distribution, which can be seen from Eq. (B2). The corresponding analog of $F(t)$ is the cumulative incidence function (commonly abbreviated as CIF), defined as

$$F_c(t) = \int_0^t h_c(t')S(t')dt'. \quad (\text{B5})$$

$F_c(t)$ is the cause-specific failure before time t , taking into account the condition that competing failure causes have not taken place. This function has the property $F(t) = \sum_c F_c(t)$ due to the linearity of the previous definitions.